Monthly Notices
of the
ROYAL ASTRONOMICAL SOCIETY

MNRAS **00,** 1 (2020)
Advance Access publication 2020 September 9

doi:10.1093/mnras/staa2196

High molecular gas content and star formation rates in local galaxies that host quasars, outflows, and jets

M. E. Jarvis [1,2,3★] C. M. Harrison [4★] V. Mainieri [2] G. Calistro Rivera [2] P. Jethwa [5] Z.-Y. Zhang [6] D. M. Alexander,[7] C. Circosta,[8] T. Costa,[1] C. De Breuck [2] D. Kakkad,[9] P. Kharb [10] G. B. Lansbury [2] and A. P. Thomson[11]

[1]*Max-Planck Institut für Astrophysik, Karl-Schwarzschild-Str. 1, D-85748 Garching, Germany*
[2]*European Southern Observatory, Karl-Schwarzschild-Str. 2, D-85748 Garching, Germany*
[3]*Ludwig Maximilian Universität, Professor-Huber-Platz 2, D-80539 Munich, Germany*
[4]*School of Mathematics, Statistics and Physics, Newcastle University, Newcastle upon Tyne NE1 7RU, UK*
[5]*Institut für Astrophysik, Universität Wien, Türkenschanz-Str. 17, A-1180 Vienna, Austria*
[6]*School of Astronomy and Space Science, Xianlin Campus, Nanjing University, 163 Xianlin Avenue, Nanjing, Jiangsu 210093, China*
[7]*Centre for Extragalactic Astronomy, Department of Physics, Durham University, South Road, Durham DH1 3LE, UK*
[8]*Dept of Physics & Astronomy, University College London, Gower Street, London WC1E 6BT, UK*
[9]*European Southern Observatory, Alonso de Cordova, 3107, Vitacura Casilla 19001, Santiago, Chile*
[10]*National Centre for Radio Astrophysics – Tata Institute of Fundamental Research, Pune University Campus, Post Bag 3, Ganeshkhind, Pune 411007, India*
[11]*Jodrell Bank Centre for Astrophysics, Department of Physics and Astronomy, The Alan Turing Building, Upper Brook Street, Manchester M13 9PL, UK*

Accepted 2020 July 17. Received 2020 July 2; in original form 2020 June 1

ABSTRACT

We use a sample of powerful $z \approx 0.1$ type 2 quasars ('obscured'; $\log[L_{\rm AGN}/{\rm erg\,s^{-1}}] \gtrsim 45$), which host kpc-scale ionized outflows and jets, to identify possible signatures of AGN feedback on the total molecular gas reservoirs of their host galaxies. Specifically, we present Atacama Pathfinder EXperiment (APEX) observations of the CO(2–1) transition for nine sources and the CO(6–5) for a subset of three. We find that the majority of our sample reside in starburst galaxies (average specific star formation rates – sSFR – of 1.7 Gyr^{-1}), with the seven CO-detected quasars also having large molecular gas reservoirs (average $M_{\rm gas} = 1.3 \times 10^{10}$ M$_\odot$), even though we had no pre-selection on the star formation or molecular gas properties. Despite the presence of quasars and outflows, we find that the molecular gas fractions ($M_{\rm gas}/M_\star = 0.1$–$1.2$) and depletion times ($M_{\rm gas}$/SFR = 0.16–0.95 Gyr) are consistent with those expected for the overall galaxy population with matched stellar masses and sSFRs. Furthermore, for at least two of the three targets with the required measurements, the CO(6–5)/CO(2–1) emission-line ratios are consistent with star formation dominating the CO excitation over this range of transitions. The targets in our study represent a gas-rich phase of galaxy evolution with simultaneously high levels of star formation and nuclear activity; furthermore, the jets and outflows do not have an immediate appreciable impact on the global molecular gas reservoirs.

Key words: ISM: jets and outflows – ISM: molecules – galaxies: active – galaxies: evolution – galaxies: general – galaxies: ISM.

1 INTRODUCTION

The energy from accreting supermassive black holes (i.e. active galactic nuclei, AGN) is widely accepted to be responsible for the global quenching of star formation in massive galaxies (AGN feedback; e.g. see reviews in Alexander & Hickox 2012; Fabian 2012; Harrison 2017). However, the physical mechanisms by which this energy couples to the gas on galactic scales and its precise impact on the host galaxy remains unclear. Multiwavelength studies are proving to be vital in both determining the mechanism and impact of feedback (see e.g. Cicone et al. 2018; Cresci & Maiolino 2018).

AGN are thought to be able to remove gas from their host galaxies via outflows. These outflows can be powered by the interaction between interstellar gas and small-scale accretion disc winds (Faucher-Giguère & Quataert 2012; Zubovas & King 2012) or directly via radiation pressure on dust (Ishibashi & Fabian 2015; Thompson et al. 2015; Bieri et al. 2017; Costa et al. 2018a,b), particularly for AGN with high Eddington ratios ('quasar' or 'radiative mode'). While typically thought to operate primarily by preventing hot halo gas from cooling, via the so-called 'radio' or 'maintenance mode' (e.g. Churazov et al. 2005), collimated jets are also likely to drive outflows of interstellar gas (Wagner, Bicknell & Umemura 2012; Mukherjee et al. 2016), blurring the division between 'quasar' and 'maintenance' modes (see e.g. Jarvis et al. 2019).

In particular, the potential impact of AGN is most commonly observed through high-velocity ionized gas outflows (see e.g. Karouzos, Woo & Bae 2016; Morganti 2017; Davies et al. 2020). However, if the direct impact of AGN upon star formation is to be understood, it is the cold (∼10 K) molecular gas (primarily composed of H_2) that forms the fuel for star formation, which must be

★ E-mail: miranda.jarvis@gmail.com (MEJ);
christopher.harrison@newcastle.ac.uk (CMH)

considered (Morganti 2017). Since cold molecular gas is not directly observable in H_2 emission, carbon monoxide (^{12}CO), which has a permanent dipole moment, is most often used as a tracer of these cold molecular clouds (see e.g. Bolatto, Wolfire & Leroy 2013; Carilli & Walter 2013, and references therein). Specifically, the ground-level transition ($J = 1$–0) has an excitation temperature of just 5.53 K, making it a good tracer of the total cold molecular gas (see e.g. Bolatto et al. 2013), while higher-J CO lines (i.e. $J \gtrsim 4$–3) are produced from warmer, denser gas (see e.g. van der Werf et al. 2010; Daddi et al. 2015; Mashian et al. 2015; Kamenetzky, Rangwala & Glenn 2017).

Molecular gas outflows traced by CO gas have been identified in both radio- and quasar-mode AGN (see e.g. Cicone et al. 2014; King & Pounds 2015; Morganti et al. 2015; Bischetti et al. 2019; Fotopoulou et al. 2019; Oosterloo et al. 2019; Lutz et al. 2020; Veilleux et al. 2020). However, these outflows typically only represent ∼10 per cent of the molecular gas luminosity (see e.g. Fluetsch et al. 2019; Lutz et al. 2020) and so are difficult to observe. Instead, the impact of AGN on the molecular gas in their host galaxies is often probed through the total molecular gas content (see e.g. Bertram et al. 2007; Xia et al. 2012; Husemann et al. 2017; Rosario et al. 2018). Specifically, the gas mass and the molecular gas fraction relative to the star formation rate (SFR) are used to assess the potential impact of the AGN on the star formation efficiency and/or their ability to deplete the molecular gas supply within the host galaxies (e.g. Kakkad et al. 2017; Perna et al. 2018). In addition to removing molecular gas through outflows, AGN and mechanical feedback from jets can heat the molecular gas, which both inhibits star formation and causes the CO to emit in higher transitions (see e.g. Papadopoulos et al. 2010).

Our recent results, combining integral field spectrographic (IFS) and radio observations, have identified a sample of luminous ($L_{[\rm O\,III]} > 10^{42}$ erg s^{-1}) type 2 (obscured) AGN with signatures of jets and extended ionized gas outflows. These systems represent the ideal environment to search for signatures of feedback since they have the strong potential to interact with their environments both mechanically and radiatively (Harrison et al. 2014, 2015; Lansbury et al. 2018; Jarvis et al. 2019). In this work, we use unresolved CO measurements of the (2–1) and (6–5) transitions, to investigate the molecular gas content of these systems and look for signatures of the impact of the AGN and jet in particular, through thermal excitation and depletion of the gas reservoir.

In Section 2, we introduce our sample, describe our spectral energy distribution (SED) fitting approach used to determine key galaxy and AGN properties (Section 2.1), and compare our sample to the star-forming main sequence (Section 2.2). Section 3 describes our data, data reduction (Section 3.1), and analysis (Section 3.2). In Section 4, we describe our results, and in Section 5, we compare the total molecular gas and CO excitation in our systems to literature results (Sections 5.1 and 5.2, respectively) and we discuss these results in the wider context of galaxy evolution in Section 5.3. We present our conclusions in Section 6. We adopt $H_0 = 70$km s^{-1}Mpc^{-1}, $\Omega_{\rm M} = 0.3$, $\Omega_\Lambda = 0.7$ throughout, and assume a Chabrier (2003) initial mass function (IMF).

2 SAMPLE SELECTION AND PROPERTIES

Here we present observations of the molecular gas in nine type 2 quasars. This sample was designed to be representative of powerful local AGN, with signatures of feedback, and therefore is ideal for identifying the impact of the AGN on the molecular gas reservoir. In particular, by selecting sources with previously identified ionized gas outflows and radio jets, the AGN should be able to impact the molecular gas through radiative and/or mechanical feedback by exciting and/or removing the molecular gas.

In Fig. 1, we show how our targets were selected from the parent sample of 24 264 $z < 0.4$ spectroscopically identified AGN[1] presented in Mullaney et al. (2013). In Harrison et al. (2014), we selected 16 $z < 0.2$ type 2 AGN with luminous [O III] outflows: $L_{[\rm O\,III]} > 10^{41.7}$ erg s^{-1} and full width at half-maximum (FWHM) $\gtrsim$700 km s^{-1} (see Fig. 1). The only other selection criteria was an RA/Dec. cut to select sources observable from Gemini-South. Using IFS data, we revealed that these outflows are extended on $\gtrsim$kpc scales. For this work, we selected the 9 of these 16 targets with the highest [O III] luminosities (i.e. $L_{[\rm O\,III]} > 10^{42}$ erg s^{-1}) and radio luminosities ($\log[L_{1.4\rm GHz}/\rm W\,Hz^{-1}] \geq 23.5$; see Fig. 1). In Jarvis et al. (2019), we established that the radio luminosity of these targets is dominated by emission from the AGN, with eight of the nine exhibiting extended radio structures on 1–25 kpc scales, which are likely radio jets (J1010+0612 is the only target without any evidence for an extended radio structure). The spatial coincidence of these radio features to outflows and disturbed ionized gas features visible in the IFS data strongly suggests jet–gas interactions in the majority of this sample (see Harrison et al. 2015; Jarvis et al. 2019). The basic sample properties are provided in Table 1.

2.1 SED fitting

A significant amount of the analysis in this paper relies on having reliable estimates of the SFRs and stellar masses in our systems without contamination from the AGN. Since the AGN in this work are all type 2, the AGN has only a small contribution to the ultraviolet (UV)–optical emission but may still contribute significantly to the infrared (IR) emission. As such, in Jarvis et al. (2019), we performed UV–IR SED fitting using the 'Code Investigating GALaxy Emission' (CIGALE[2]; Noll et al. 2009; Buat et al. 2015; Ciesla et al. 2015) to derive the host galaxy and AGN properties of this sample. We used data from *GALEX*, SDSS, 2MASS, *WISE*, IRAS, and, where available, archival, *Herschel* PACS and SPIRE, for these SED fits, corrected for Galactic extinction (see Jarvis et al. 2019). Specifically, CIGALE simultaneously fits the attenuated stellar emission, star formation heated dust emission, AGN emission (from the accretion disc and dust heating), and nebular emission. Of particular relevance for this work are the stellar mass ($M_\star$) and the SFR of the host galaxies, which are listed in Table 1. We calculated these SFRs from the SED-derived IR luminosity due to star formation ($L_{\rm IR,\,SF}$) and the relationship from Kennicutt & Evans (2012), converting from a Kroupa into a Chabrier IMF by multiplying by 0.94 (Madau & Dickinson 2014), specifically SFR $= L_{\rm IR}/(2.57 \times 10^{43}) \times 0.94$, with $L_{\rm IR}$ in erg s^{-1} and SFR in M$_\odot$ yr^{-1}. For further details of the SED fitting, derived quantities, and uncertainties, we refer the reader to Jarvis et al. (2019).

In Table 1, the quoted uncertainties are 1σ formal errors from the CIGALE fits and do not include systematics. However, there is a 0.3-dex systematic uncertainty expected on the IR luminosity and stellar mass from the SED fitting (Gruppioni et al. 2008; Mancini et al. 2011; Santini et al. 2015). This results in a 0.42-dex systematic uncertainty for the SFR values, from adding in quadrature the systematic uncertainties from the SED fitting and the 0.3-dex systematic uncertainty on the conversion between $L_{\rm IR}$ and SFR (Kennicutt & Evans 2012). Our sources have stellar masses

[1]Using a combination of 'BPT' diagnostics (Baldwin, Phillips & Terlevich 1981), and emission-line widths.
[2]https://cigale.lam.fr.

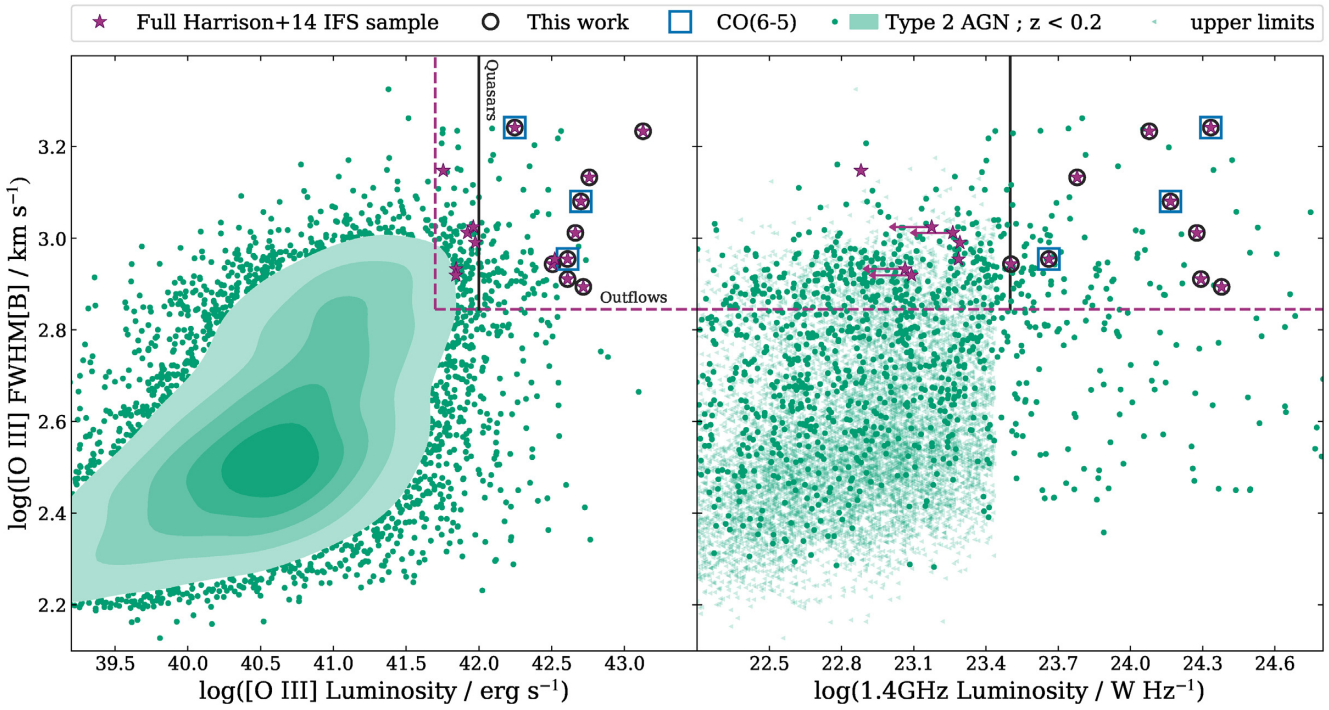

Figure 1. This figure shows the basic sample properties and selection criteria. In each panel, the full Harrison et al. (2014) sample are shown as magenta stars with the sources studied here highlighted with black circles and the APEX CO(6–5) sample additionally highlighted with blue squares (values tabulated in Jarvis et al. 2019). Our parent population of $z < 0.2$ type 2 AGN are shown as green data points and contours (Mullaney et al. 2013). The dashed magenta lines show the selection criteria used in Harrison et al. (2014) and the black solid lines mark the additional selection criteria applied for the sample in this work. Left-hand panel: the FWHM of the broadest, luminous [O III] emission-line component versus the total [O III] luminosity (see Harrison et al. 2014; Jarvis et al. 2019). Right-hand panel: the FWHM versus the radio luminosity (from FIRST fluxes), where the parent sample sources with only upper limits on their radio luminosity are shown as light green triangles.

Table 1. Target list and properties.

Name	RA (J2000)	Dec. (J2000)	z	$\log(M_\star)$ ($M_\odot$)	$\log(L_{\rm IR,\,SF})$ (erg s^{-1})	SFR ($M_\odot$ yr^{-1})	$\Delta_{\rm MS}$	[O III]/Hβ
(1)	(2)	(3)	(4)	(5)	(6)	(7)	(8)	(9)
J0945+1737	09:45:21.33	+17:37:53.2	0.1281	$10.1^{+0.09}_{-0.12}$	45.3 ± 0.02	73 ± 4	36.1	1.015 ± 0.005
J0958+1439	09:58:16.88	+14:39:23.7	0.1091	$10.74^{+0.09}_{-0.12}$	$44.6^{+0.2}_{-0.3}$	15 ± 8	2.4	1.124 ± 0.005
J1000+1242	10:00:13.14	+12:42:26.2	0.1479	$9.9^{+0.3}_{-0.7}$	$45.0^{+0.1}_{-0.2}$	40 ± 10	24.8	0.988 ± 0.008
J1010+1413	10:10:22.95	+14:13:00.9	0.1992	11.0 ± 0.1	$45.1^{+0.2}_{-0.4}$	50 ± 30	3.7	1.1 ± 0.005
J1010+0612	10:10:43.36	+06:12:01.4	0.0982	$10.5^{+0.3}_{-0.9}$	44.99 ± 0.04	35 ± 3	8.7	0.828 ± 0.005
J1100+0846	11:00:12.38	+08:46:16.3	0.1004	$10.7^{+0.3}_{-2.4}$	45.0 ± 0.1	34 ± 9	6.2	1.098 ± 0.005
J1316+1753	13:16:42.90	+17:53:32.5	0.1504	$11.0^{+0.2}_{-0.3}$	$45.1^{+0.2}_{-0.3}$	40 ± 20	4.3	1.082 ± 0.005
J1356+1026	13:56:46.10	+10:26:09.0	0.1233	$10.64^{+0.09}_{-0.11}$	45.36 ± 0.02	84 ± 4	15.3	0.982 ± 0.004
J1430+1339	14:30:29.88	+13:39:12.0	0.0852	$10.86^{+0.05}_{-0.06}$	$44.32^{+0.06}_{-0.07}$	8 ± 1	1.0	0.883 ± 0.004

Notes. (1) Object name; (2)–(3) optical RA and Dec. positions from SDSS (DR7); (4) Systemic redshifts from GMOS IFS data ([O III]; Jarvis et al. 2019); (5)–(8) are directly from, or are derived from, the CIGALE SED fits first presented in Jarvis et al. (2019) and discussed here in Section 2.1: (5) stellar mass from SED fitting (there is an additional ∼0.3 dex systemic uncertainty not included in the quoted errors), (6) infrared (IR) luminosity from star formation in the range 8–1000 μm (i.e. excluding the AGN contribution; there is a ∼0.3 dex systemic uncertainty not included in the quoted errors), (7) SFR calculated from $L_{\rm IR,\,SF}$ (there is an ∼0.42 dex systematic uncertainty not included in the quoted errors; see Section 2.1), (8) distance of the source from the Sargent et al. (2014) main sequence, defined as sSFR/sSFR$_{\rm MS}$ (see Section 2.2); (9) ratio of the [O III]5007 to Hβ emission lines from SDSS DR7 catalogues (single Gaussian fits; Abazajian et al. 2009). Additional details of these sources (e.g. radio luminosity and AGN bolometric luminosity) are given in Jarvis et al. (2019).

in the range $8 \times 10^9 < M_\star < 1.1 \times 10^{11}$ M$_\odot$ and SFRs in the range $8 < {\rm SFR} < 84$ M$_\odot$yr^{-1}. All but one of our sources (J1430+1339) are classified as luminous infrared galaxies (LIRGs) based upon their IR luminosities due to star formation (10^{11}–10^{12} $L_\odot$; see Fig. 2).

We verified these values by performing independent SED fits using another code: AGNFITTER (Calistro Rivera et al. 2016). The main difference between this code and the CIGALE code is that CIGALE assumes an energy balance between the IR and optical emission for the host galaxy, where AGNFITTER considers the two almost independently with a prior that the energy from the IR must be at least equal to the energy attenuated from the stellar emission. For the three of our sources with *Herschel* observations, which have the

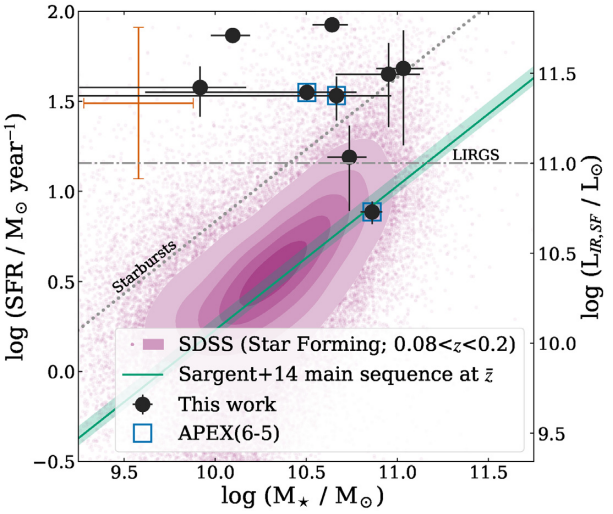

Figure 2. Our sources compared to the star-forming main sequence, as shown by the comparison of stellar mass ($M_\star$) and SFR. Our sample is shown as black circles and the APEX CO(6–5) sample is highlighted with blue squares. The red error bar in the top left-hand corner shows the systematic errors (see Section 2.1). The magenta contours and small translucent points show values for star-forming galaxies from SDSS. The solid green line shows the main sequence as given in Sargent et al. (2014) at the mean redshift of our sources ($z = 0.127$), with the width showing the variation across the redshift spanned by our sources. The grey dotted line marks the region occupied by starbursts ($\Delta_{MS}>4$) and the grey dot–dashed lines mark the limit for LIRGs ($L_{IR} \geq 10^{11}\ L_\odot$). All of our sources lie on or above the main sequence with seven being classified as starbursts.

best available coverage of the FIR emission (namely J1100+0846, J1356+1026, and J1430+1339; see Jarvis et al. 2019), the IR-derived SFRs agree within 0.27 dex (i.e. within the systematic uncertainty). For the remaining six sources, the best SFR from AGNFITTER is based on the optical emission alone and as such is a lower limit on the actual SFR (Calistro Rivera et al. 2016). In each case, this limit is consistent with our SFR from CIGALE. The stellar masses from AGNFITTER are, on average, 0.19 dex higher than those from CIGALE (i.e. within the systematic uncertainty), and the only significant outliers are J1000+1242 and J1010+0612, which have AGNFITTER-derived stellar masses 0.67 and 0.48 dex larger than those from CIGALE, respectively. We note that using the AGNFITTER stellar masses and SFRs would not change the main conclusion of this work. In summary, we trust the CIGALE SED-derived stellar masses and SFRs used throughout this work, within the limitations of the unavoidable systematic uncertainties discussed above.

2.2 Our targets in the context of the star-forming main sequence

There is a long established trend observed between SFR and stellar mass for star-forming galaxies, which is commonly referred to as the 'star-forming main sequence' (see e.g. Brinchmann et al. 2004; Daddi et al. 2007; Elbaz et al. 2007; Noeske et al. 2007; Salim et al. 2007; Wyder et al. 2007). This relation provides a useful comparison to put our sample into the wider context of star-forming galaxies. Specifically, we consider where our galaxies lie in comparison to the redshift-dependent main sequence of Sargent et al. (2014, see Fig. 2). We chose this parametrization as it visually provided the best fit to galaxies selected from SDSS (the parent sample of our work), where the other main sequences checked were Bauermeister et al. (2013), Speagle et al. (2014), Whitaker et al. (2014), Genzel et al. (2015), and Schreiber et al. (2015). In Fig. 2, we show the Sargent et al. (2014) main sequence compared to all SDSS sources defined as star forming based on BPT emission-line ratios (Kauffmann et al. 2003; Brinchmann et al. 2004; Tremonti et al. 2004) within $z = 0.08$–0.2 (i.e. the redshift range spanned by our sources) using the MPA-JHU measurements[3] converted from a Kroupa into Chabrier IMF (Madau & Dickinson 2014). We define the distance from the main sequence (Δ_{MS}) for each source as the ratio of its specific star formation rate (sSFR $\equiv$ SFR/$M_\star$) compared to that of the main sequence at its redshift and stellar mass (Sargent et al. 2014). Following the literature, we define our targets as 'starbursts' if they have $\Delta_{MS} > 4$ (see e.g. Elbaz et al. 2011); however, we note that we use this definition for a comparison to the overall population only and do not claim that they are physically different to the rest of the population for this work.

Using the definitions described above, all of our sources are on or above their local main sequence with seven classified as starbursts,[4] even though we applied no pre-selection on SFR or IR luminosity (see Table 1).

3 OBSERVATIONS AND DATA REDUCTION

3.1 Data reduction

We use the Atacama Pathfinder EXperiment (APEX) to observe the spatially unresolved molecular gas emission in the CO(2–1) and CO(6–5) transitions. We observed CO(2–1) for the whole sample presented here and CO(6–5) for a representative subsample (J1010+0612, J1100+0846, and J1430+1339; see Figs 1 and 2). These specific transitions were selected based on a combination of scientific and observational constraints. Specifically, lower CO transitions (CO(1–0) in particular) are best used to trace the total cold molecular gas content (e.g. Bolatto et al. 2013; Carilli & Walter 2013) and the CO(2–1) transition is the lowest observable at the redshift of our targets with the available APEX instrumentation. Higher CO transitions trace molecular gas that has been excited by star formation, shocks and the AGN (e.g. Mashian et al. 2015; Carniani et al. 2019; Vallini et al. 2019). Specifically, the CO(6–5) transition was selected based on indications that it can be boosted by AGN activity and jets in particular (Papadopoulos et al. 2010), and because it was the highest transition that could be observed for our targets in a reasonable time using APEX, due to available instrumentation and the atmospheric transmission. Due to observing constraints (e.g. the need for good weather for these observations; see Table 2), we only observed three of our targets in CO(6–5); however, these three are representative of the overall population (see Figs 1 and 2).

We observed CO(2–1) for our targets under proposal id. E-0100.B-0166 [PI: Jarvis] with the observations carried out between 2017 July 7 and 2018 December 29 with precipitable water vapours (PWVs) between 0.6 and 4.7 mm. Three different instruments were used for these observations due to the redshift range of the targets and changes in the available instrumentation over the period of observation, namely the Swedish-ESO PI receiver for APEX (SEPIA180; Belitsky et al. 2018), the Max Planck Institute for Radio Astronomy's PI230, and the APEX-1 receiver (SHeFI 230-GHz band; Vassilev et al. 2008). The instrument used for each source, the dates they were observed, and the PWV values during the observations are listed

[3] https://www.sdss.org/dr12/spectro/galaxy_mpajhu/.

[4] J1010+1413 is right on the transition between normal star forming and starburst with $\Delta_{MS} = 3.7$. In the rest of this paper, we assume Δ_{MS}~4 and consider it as a starburst.

Table 2. Details of the observations.

Target	Instrument	t_{on} (min)	Date	K Jy^{-1}	PWV (mm)
(1)	(2)	(3)	(4)	(5)	(6)
CO(2–1); proposal id. E-0100.B-0166 [PI: Jarvis]					
J0945+1737	SEPIA180	126	2018-10-24	36 ± 5	0.7
			2018-11-11	36 ± 5	1.4
			2018-12-27	36 ± 5	2.1
			2018-12-28	36 ± 5	4.7
			2018-12-29	36 ± 5	3.0
J0958+1439	SEPIA180	71.6	2018-10-26	36 ± 5	0.6
			2018-12-27	36 ± 5	2.1
			2018-12-28	36 ± 5	4.7
J1000+1242	SEPIA180	261	2018-10-24	36 ± 5	0.7
			2018-11-01	36 ± 5	1.3
			2018-11-02	36 ± 5	1.3
			2018-11-04	36 ± 5	1.5
			2018-11-05	36 ± 5	0.7
			2018-11-08	36 ± 5	0.9
J1010+1413	SEPIA180	28.5	2018-10-26	36 ± 5	0.6
			2018-10-31	36 ± 5	0.9
			2018-11-02	36 ± 5	1.3
			2018-11-03	36 ± 5	1.5
J1010+0612	PI230	167	2018-10-29	42 ± 6	0.8
J1100+0846	SEPIA180	51.4	2017-07-27	40 ± 6	0.9
			2018-11-03	36 ± 5	1.5
J1316+1753	SEPIA180	78.5	2017-07-28	40 ± 6	0.9
			2018-12-28	36 ± 5	4.7
J1356+1026	SEPIA180	35.8	2017-07-27	40 ± 6	0.9
			2017-07-28	40 ± 6	0.8
J1430+1339	APEX-1	101	2017-07-29	38 ± 6	0.7
			2017-07-30	38 ± 6	0.9
			2017-07-31	38 ± 6	1.0
			2017-08-02	38 ± 6	0.7
			2017-08-03	38 ± 6	0.9
			2017-08-31	38 ± 6	1.7
			2017-09-01	38 ± 6	1.6
CO(6–5); proposal id. E-0104.B-0292 [PI: Harrison]					
J1010+0612	SEPIA660	145.2	2019-10-29	69 ± 6	0.5
J1100+0846	SEPIA660	220.6	2019-11-05	69 ± 6	0.4
			2019-11-06	69 ± 6	0.4
			2019-12-10	69 ± 6	0.5
J1430+1339	SEPIA660	118	2019-08-31	69 ± 6	0.6

Notes. (1) Object name; (2) instrument; (3) on source time of the final total spectrum; (4) date observed (year-month-day); (5) conversion factor used to convert the observed antenna temperature (in K) into flux density (in Jy); (6) average precipitable water vapour (PWV; mm) during the observations. This table is divided into two parts with the details of our APEX CO(2–1) data given first and our CO(6–5) data at the bottom.

in Table 2. The CO(6–5) data were observed under proposal id. E-0104.B-0292 [PI: Harrison] and observed between 2019 August 31 and December 10 using the SEPIA660 band 9 instrument with PWVs between 0.4 and 0.6.

The data were reduced and analysed using the Continuum and Line Analysis Single-dish Software (CLASS; version mar19a).[5] For many of our sources, spectral spikes (due to bad channels) were found in at least one polarization. To correct for this while losing the minimum amount of data for each source, for each day of observations, we examined the average spectrum from each of the spectrometers separately and flagged, by eye, any channels affected by spikes. We also flagged the leading 150 channels (80 for the CO(6–5) data) and trailing 10 (in the overlap region) of each individual spectra. We combined the two spectrometers in the same sideband and polarization using Zhiyu Zhang's CLASS extension file, combineTwoIFsAPEX.class, which is made available online at https://github.com/ZhiyuZhang/gildas_class_libraries. From each of these combined scans, we subtracted a linear baseline using the CLASS BASE command, excluding a velocity range ∼500 km s^{-1} to either side of the observed line position or the expected line position from the SDSS redshift if no line was obviously seen in the total binned spectrum. We then removed scans with poor baselines based on the ratio of their rms in 50 km s^{-1} bins (selected to best reveal the baselines) compared to the theoretical rms (rms$_t$) calculated by the following equation:

$$\mathrm{rms}_t \equiv \frac{T_{\mathrm{sys}}}{\sqrt{|d\nu \times 10^6 \times t|}}, \quad (1)$$

where T_{sys} is the system temperature, t is the integration time, and $d\nu$ is the frequency step size. The cutoff value for each was selected based on a combination of visual examination and minimizing the resultant final rms of the combined data in 100 km s^{-1} bins (selected to best reveal the emission lines) and ranged from rms/rms$_t$ = 1.25–2. Each day's data were then multiplied by the appropriate Kelvin to Jansky conversion factor. For each time frame and instrument, the K Jy^{-1} conversion was determined using the APEX telescope efficiencies tool (http://www.apex-telescope.org/telescope/efficiency/), supplemented by private communications with Juan–Pablo Perez–Beaupuits (see Table 2 for the values used). Finally, the spectra were combined into a single spectrum and re-sampled to 1 km s^{-1} bins with a final linear baseline removed.

We show the final reduced APEX data in the velocity range around the CO(2–1) emission line in Fig. 3 and around the CO(6–5) emission line in Fig. 4.

3.2 Data analysis

We fit each averaged spectrum using Bayesian fitting and MCMC implemented through EMCEE (Foreman-Mackey et al. 2013).[6] This Bayesian method is preferred over frequentist fitting techniques for this analysis since it is less sensitive to binning, provides realistic uncertainties, and for the upper limits in particular requires only minimal assumptions on the line profile (see Appendix A). We assume a single Gaussian profile for the line, and fit for the line flux (f; integral under the line), peak velocity (v_p, central line velocity offset from the systemic redshift in Table 1), and standard deviation (σ; the width of the line) as well as the standard deviation of the noise in the spectrum (σ_{N}), which we assume to be Gaussian. The results of the fitting are listed in Table 3 and shown in Figs 3 and 4. The full details of this analysis are given in Appendix A.

3.3 Evaluating contamination from other sources and beam corrections

The beams of the APEX observations discussed here are ∼28 arcsec (∼52 kpc at a representative redshift of $z = 0.1$) for the CO(2–1) data and ∼9 arcsec (∼17 kpc at $z = 0.1$) for the CO(6–5) data. Based on the relatively large beams of the APEX data and considering the optical sizes of our targets, we do not expect any CO flux to fall beyond our observed beams, making beam corrections unnecessary.

[5]From the GILDAS software package: http://www.iram.fr/IRAMFR/GILDAS/.

[6]http://dfm.io/emcee/current/.

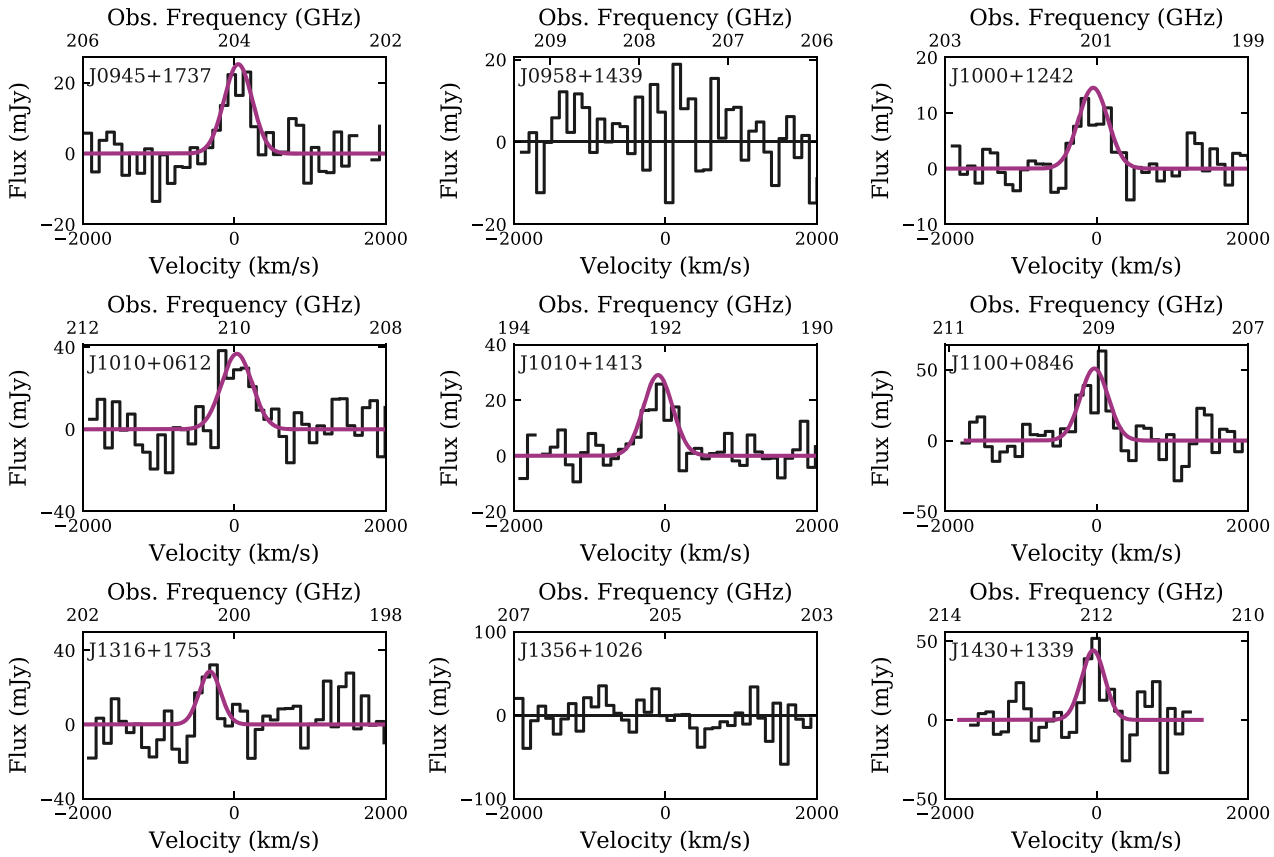

Figure 3. Our APEX CO(2–1) data (black curve) for each source. Overplotted for each is the results of our Bayesian fitting to the emission line, specifically the Gaussian constructed from the 50th percentile value from the posteriors for each parameter (magenta; see Table 3). For the two non-detections, a black horizontal line at flux = 0 is plotted to help guide the eye.

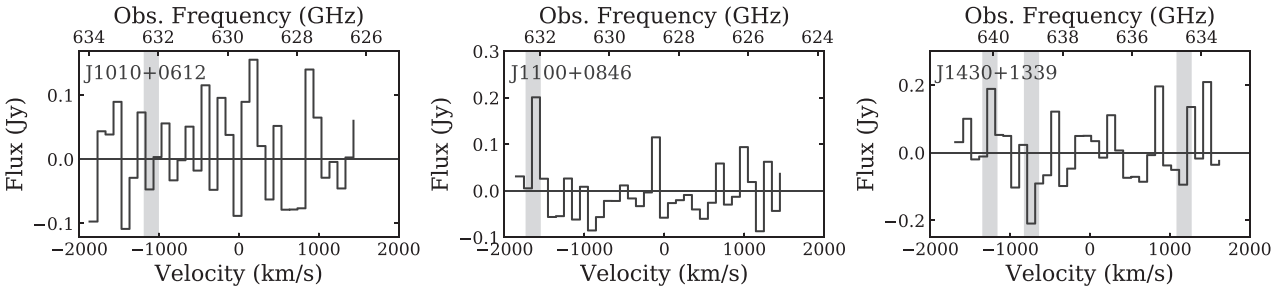

Figure 4. Our APEX CO(6–5) data. All three are undetected. Grey vertical bands highlight frequencies where there are narrow atmospheric absorption features that can cause slightly higher noise. A black horizontal line at flux = 0 is plotted to help guide the eye.

However, the large CO(2–1) beam raises the possibility that other CO bright objects may be contaminating our flux measurements. To check for this scenario, we used higher spatial resolution ALMA CO observations. Specifically, we use the CO(1–0) and CO(3–2) images published in Sun et al. (2014) for J1356+1026, and for the other targets, we use preliminary CO(3–2) images from two proposals carried out by our group[7] that have a spatial resolution of ∼0.3–0.5 arcsec and a maximum recoverable scale of ∼4 arcsec.[8] The only target where a possible contaminating CO source was identified is J1010+0612 that has a CO(3–2) bright companion ∼7 arcsec away, which is within our CO(2–1) beam. Preliminary flux measurements from the ALMA data reveal that ∼82 per cent of the total flux is in our primary target of J1010+0612, a difference that is within the

[7]Specifically, id. 2016.1.01535.S (PI: Lansbury), and id. 2018.1.01767.S (PI: Thomson).

[8]For J1430+1339, the ALMA data have a maximum recoverable scale of ∼19 arcsec.

Table 3. CO emission-line measurements.

Name	f (Jy km s^{-1})	v_p (km s^{-1})	σ (km s^{-1})	σ_N (Jy)	L'_{CO} ($1 \times 10^9 \times$ K km s^{-1} pc^2)
(1)	(2)	(3)	(4)	(5)	(6)
CO(2–1)					
J0945+1737	12 ± 2	50^{+50}_{-40}	180^{+50}_{-40}	0.062	$2.3^{+0.5}_{-0.4}$
J0958+1439	<21.5	–	–	0.086	<3.0
J1000+1242	7 ± 1	-40 ± 40	200^{+40}_{-30}	0.031	1.9 ± 0.3
J1010+1413	14 ± 2	-100 ± 30	190^{+40}_{-30}	0.11	7 ± 1
J1010+0612[a]	19 ± 4	30^{+60}_{-50}	200^{+60}_{-50}	0.052	$2.1^{+0.5}_{-0.4}$
J1100+0846	23 ± 4	-30 ± 40	180^{+40}_{-30}	0.12	2.8 ± 0.4
J1316+1753	10^{+5}_{-4}	-320^{+90}_{-60}	140^{+110}_{-50}	0.13	3 ± 1
J1356+1026	<33.1	–	–	0.23	<6.0
J1430+1339	17 ± 5	-40^{+60}_{-50}	150^{+60}_{-40}	0.16	1.4 ± 0.4
CO(6–5)					
J1010+0612	<110	–	–	0.56	<1.4
J1100+0846	<74	–	–	0.48	<0.98
J1430+1339	<135	–	–	0.90	<1.2

Notes. (1) Object name; (2–5) are values derived from our Bayesian fits to the APEX data, consisting of the 50th percentile (median) value with errors derived from the 16th and 84th percentiles: (2) line flux in Jy. For non-detections, 3σ upper limits are given; (3) peak velocity in km s^{-1} with respect to the systematic redshift given in Table 1; (4) width of the line as a standard deviation in km s^{-1}; (5) standard deviation of the noise in the final 1 km s^{-1} binned spectrum (see Section 3.2); (6) $L'_{CO}/10^9$ in K km s^{-1} pc^2. This table is divided into two parts with the details of our fits to the APEX CO(2–1) data given first, and then our fits to the CO(6–5) data are in the bottom portion.
[a]Due to a nearby CO bright companion that is included within the CO(2–1) beam, the true CO(2–1) flux of this source could be up to 18 per cent lower than the value given here (see Section 3.3); the other line parameters are not used in the discussion of this paper.

1σ error bars from our Bayesian fit.[9] We highlight this source in subsequent figures.

4 RESULTS

We show the final reduced APEX data, in 100 km s^{-1} bins, around the CO(2–1) line (for all nine targets) in Fig. 3 and around the CO(6–5) line in Fig. 4 (for the three targets observed). In the online supplementary data for this paper we provide corner plots displaying the posterior probability distributions of each of the parameters for each source. For the CO(2–1) data, all but J0958+1439 and J1356+1026 show distinct peaks in the probability distribution for each parameter, indicating a detection. Therefore, we detect seven of our nine targets in CO(2–1). None of the three sources observed in CO(6–5) show distinct peaks in the posterior probability distributions of all parameters and are clearly undetected.

For the detected emission lines, we quote the 50th percentile (median) of the posterior distribution for each parameter in Table 3, and use the 16th and 84th percentile as errors. We note there is an additional ∼13 per cent systematic uncertainty on the line flux from the error on the temperature to flux density conversion factors (Section 3.1). The values derived from our Bayesian analysis are consistent within errors to those derived from fitting a Gaussian directly to the data in 100 km s^{-1} bins. In Fig. 3, we show the resulting line profiles from our Bayesian procedure as Gaussians constructed using the 50th percentile value for each parameter. These parameter values will be adopted for the analyses throughout this work.

[9]This is supported by the per cent of the total system flux in J1010+0612 from 2MASS, which is 87, 92, and 91 per cent, of the combined fluxes of these two sources, in the J, H, and K_s bands, respectively.

For the non-detected emission lines, we derived 3σ upper limits on the line flux from the 99.7th percentile on the posterior distribution (see values in Table 3). Our upper limit for J1356+1026 (i.e. $L'_{CO(2-1)} < 6 \times 10^9$ K km s^{-1} pc^2) is consistent with the observed value obtained by converting the total L'_{CO}(1–0) reported for this source in Sun et al. (2014) into CO(2–1) (i.e. $L'_{CO}(2-1) = 0.82 \times 10^9$ K km s^{-1} pc^2), where we have assumed $L'_{CO}(2-1)/(1-0) \equiv r_{21} = 0.8$ (see Section 5.1.2 for a discussion of the choice of r_{21}). J1356+1026 is discussed in more detail in Sections 5.1 and 5.3. We have no prior knowledge of the total CO emission for J0958+1439.

Overall, we detect the CO(2–1) line for seven of our nine targets with fluxes in the range 7–23 Jy km s^{-1}. The two non-detected targets have upper limits of 21.5 and 33.1 Jy km s^{-1} (for J0958+1439 and J1356+1026, respectively). Our upper limits on the CO(6–5) fluxes are 110, 74, and 135 Jy km s^{-1} for J1010+0612, J1100+0846, and J1430+1339, respectively. For the CO(2–1) detections, we measured peak line velocities between −320 and 50 km s^{-1} relative to the systematic redshifts in Table 1, and line widths (σ) between 150 and 200 km s^{-1}; however, we defer a discussion of the molecular gas kinematics to future work.

We calculate the CO luminosities (following e.g. Solomon et al. 1997) for each source using

$$L'_{CO}(\mathrm{K\,km\,s^{-1}pc^2}) = \frac{3.25 \times 10^7}{\nu^2_{co,rest}} \left(\frac{D_L^2}{1+z}\right) f, \quad (2)$$

where D_L is the luminosity distance in Mpc, $\nu_{co,\,rest}$ is the rest-frame frequency of the CO line in GHz (230.538 and 691.473 GHz for the CO(2–1) and CO(6–5) lines, respectively), and f is the flux of the CO line in Jy km s^{-1}. This results in $L'_{CO}(2-1)$ values of (1.4–7)$\times 10^9$ K km s^{-1} pc^2 for the seven detected sources (see Table 3). These are plotted as a function of IR luminosity in Fig. 5 and are discussed in the following section.

5 DISCUSSION

In this work, we look for signatures of AGN feedback on the molecular gas in our quasar sample. They are luminous AGN with ionized outflows and jets that may be able to impact upon the gas supply either radiatively or mechanically (see e.g. Harrison 2017 for a review). We stress that although molecular outflows are commonly observed directly through broad, generally blueshifted emission-line components (see e.g. Fluetsch et al. 2019; Lutz et al. 2020); they are typically weak in CO emission (contributing $\lesssim$10 per cent of the total emission-line profile), which would be undetectable in our data. Here we focus on the galaxy-wide molecular gas content (Section 5.1) and CO excitation (Section 5.2) of our sample of extreme quasars and compare them to redshift-matched literature galaxy samples both with and without AGN.

5.1 Molecular gas content

In order to assess if our AGN have depleted their host galaxies' gas reservoir or decreased their star formation efficiency, we compare our results to studies of general galaxy populations and other AGN samples. Specifically, we consider (1) their total CO luminosities ($L'_{\rm CO}$) compared to their IR luminosities ($L_{\rm IR}$; corrected for the AGN contribution; Section 5.1.1); (2) how the molecular gas fractions ($M_{\rm gas}/M_\star$) and depletion times ($M_{\rm gas}$/SFR) compare to other samples when SFRs, stellar masses, and offsets from the star-forming main sequence ($\Delta_{\rm MS}$) are taken into account (Section 5.1.2); and (3) the relationship between AGN properties and the molecular gas content and star formation of the host galaxy (Section 5.1.3).

5.1.1 $L'_{CO\text{-}LIR}$ relations

The correlation of $L'_{\rm CO}$ (which traces the molecular gas mass) and $L_{\rm IR}$ (which traces star formation) in star-forming galaxies is well studied (e.g. Kennicutt 1998; Genzel et al. 2010; Greve et al. 2014; Sargent et al. 2014). By directly comparing observable quantities, this analysis removes many of the assumptions that are needed to convert these values into physical parameters. A complication to this analysis, which is not always accounted for, is that AGN can contribute significantly to the IR emission (see e.g. Kirkpatrick et al. 2019). The careful SED fitting technique implemented in our work allows us to reliably consider only the IR luminosity from the star formation component, which is free from AGN contamination (i.e. $L_{\rm IR,\,SF}$; see Section 2.1).

Numerous works have parametrized the $L'_{\rm CO}$–$L_{\rm IR}$ relation using different samples of galaxies and different CO transitions. Here we focus on the work of Sargent et al. (2014), which used CO observations of 130 $z < 3$ massive ($M_\star > 10^{10}$ M$_\odot$) star-forming and starburst galaxies collected from a range of surveys. The size of the Sargent et al. (2014) sample and its coverage of similar galaxy properties as in this work make it an ideal comparison sample. They find a redshift-invariant log-linear relation between the $L'_{\rm CO}$ and $L_{\rm IR}$. We convert their relation from CO(1–0) into CO(2–1) using $r_{21} = 0.8$ (Leroy et al. 2009; Sargent et al. 2014; Daddi et al. 2015; Tacconi et al. 2018).[10] We compare the $L'_{\rm CO}$ and $L_{\rm IR}$ values for the nine targets in our sample to this relation in Fig. 5.

[10]Sargent et al. (2014) use $r_{21} = 0.8$ to convert from observed CO(2–1) into CO(1–0) in their analysis (where needed). Possible biases introduced by the choice of r_{21} are discussed in Section 5.1.2.

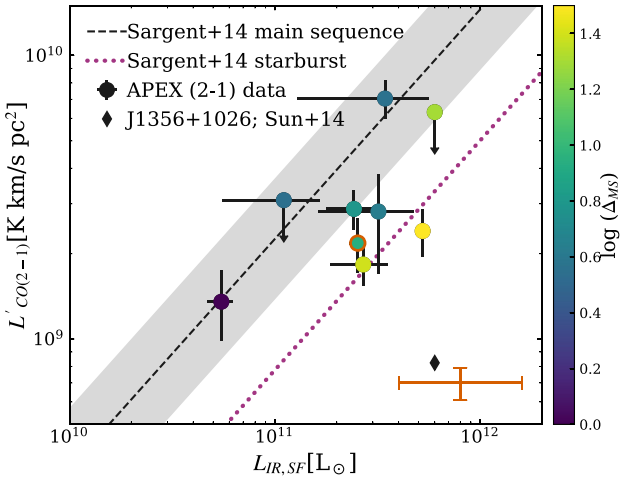

Figure 5. $L'_{\rm CO}$(2–1) compared to the IR emission produced by dust-heated star formation between 8 and 1000 μm ($L_{\rm IR,\,SF}$; see Section 2.1). Our sample are shown as circles, colour-coded by their distance from the main sequence ($\Delta_{\rm MS}$; see Section 2.2). In the bottom right-hand corner is a representative error bar showing the systematic uncertainties (see Sections 2.1 and 4). The Sun et al. (2014) value for $L'_{\rm CO}$(1–0), converted to (2–1) using $r_{21} = 0.8$, for J1356+1026 is shown as a black diamond. The black dashed and magenta dotted lines show the relationships from Sargent et al. (2014) for main sequence and starburst galaxies, respectively (see Section 5.1.1). Our quasars appear to follow the trend of star-forming galaxies, with those further from the main sequence agreeing more closely with starburst relation. J1010+0612 is highlighted with a red outline because the $L'_{\rm CO}$ may be $\lesssim$18 per cent overestimated (see Section 3.2).

We find that two out of the seven CO(2–1) detected quasars are consistent with the $L'_{\rm CO}$–$L_{\rm IR}$ relationship for main-sequence star-forming galaxies, whilst the other five have $L'_{\rm CO}$ values up to a factor of $\sim$4 lower than the relation would predict for their $L_{\rm IR}$ (see Fig. 5). However, as highlighted by the colour scaling in Fig. 5, all of the targets with low $L'_{\rm CO}$ compared to the Sargent et al. (2014) main-sequence relationship have high SFRs in relation to the main sequence (i.e. they have high $\Delta_{\rm MS}$ values; see Section 2.2). This is consistent with Sargent et al. (2014), who find that starbursts are offset to lower $L'_{\rm CO}$values by a factor of $\sim$2.9, on average, compared to main-sequence galaxies (see dotted line in Fig. 5). Indeed, all of our quasars which fall below the $L'_{\rm CO}$–$L_{\rm IR}$ relationship for main sequence galaxies are classified as starbursts (i.e. $\Delta_{\rm MS} \gtrsim 4$) and fall within 0.3 dex of the Sargent et al. (2014) relationship for starburst galaxies. We note that similar results are found when comparing our sample to the LIRG and merger $L'_{\rm CO}$–$L_{\rm IR}$ relationships of Greve et al. (2014) and Genzel et al. (2010), respectively.

Based on our data, the two CO(2–1) non-detected targets could still be consistent with the expected relationships for star-forming galaxies (the main sequence and starburst relations for J0958+1439 and J1356+1026, respectively), but could also lie significantly lower. Specifically, we note that using the Sun et al. (2014) CO(1–0) luminosity for J1356+1026 would place it approximately four times lower than the Sargent et al. (2014) starburst relation (see Fig. 5). This source is discussed in more detail in Sections 5.1.2 and 5.3.

In summary, we find that at least seven of our nine targets have $L'_{\rm CO}$ values consistent with those of the star-forming galaxy population at matched IR luminosities and at similar distance to the main sequence.

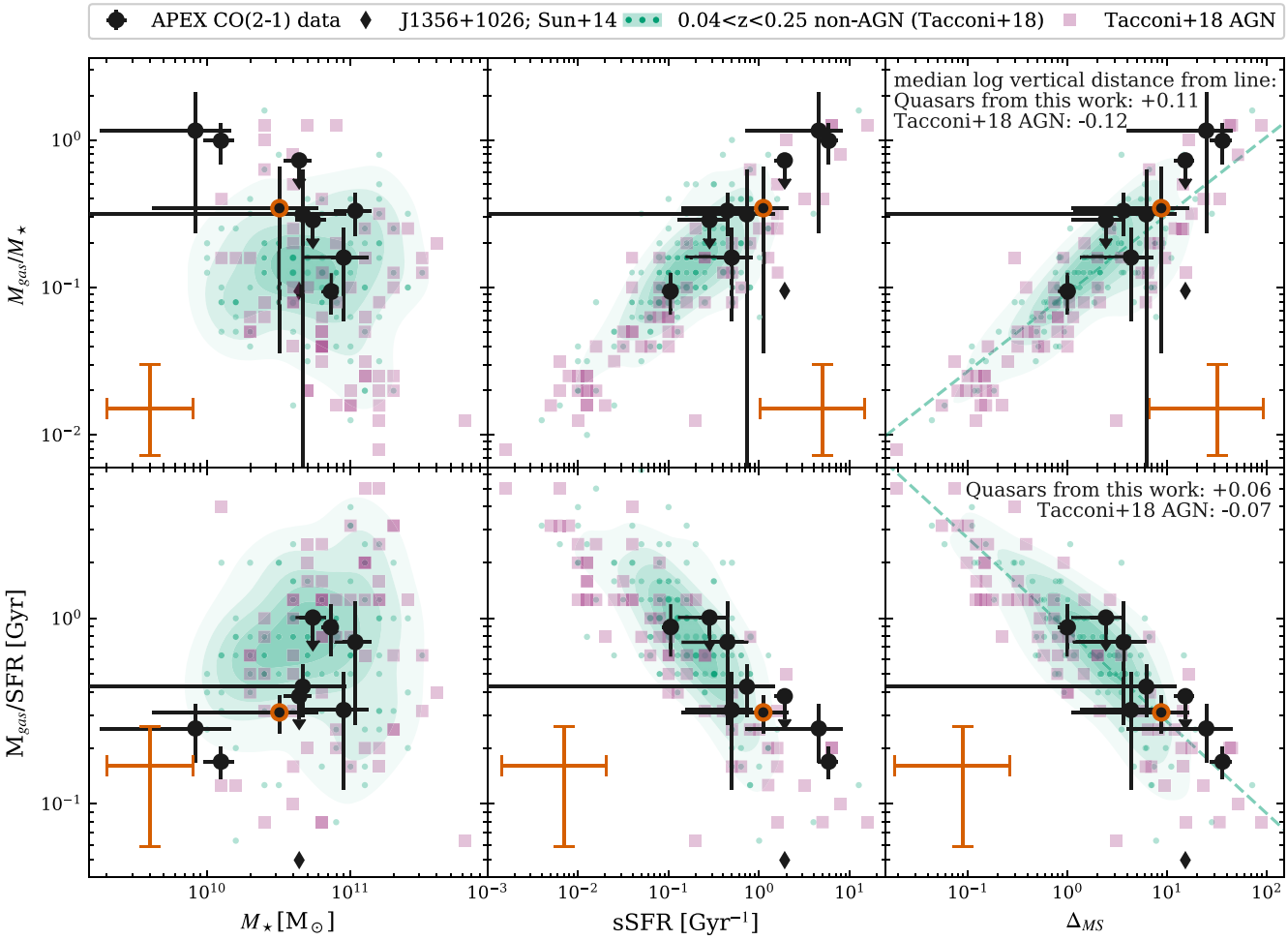

Figure 6. A comparison of the molecular gas content of our quasars (black circles) to literature values taken from Tacconi et al. (2018), within z ±0.05 of the full range of redshifts spanned by our sample. Galaxies without an identified AGN are represented by green points and density contours and AGN host galaxies by magenta squares (see Section 5.1.2). We show how the molecular gas fractions ($M_{\rm gas}/M_\star$; top panels) and depletion times ($M_{\rm gas}$/SFR; bottom panels) vary with stellar mass ($M_\star$; left-hand panels), sSFR (middle panels), and distance to the main sequence ($\Delta_{\rm MS}$; right-hand panels; see Section 2). J1010+0612 is highlighted with a red circle following Fig. 5 and a black diamond in each panel marks the value for J1356+1026 using $L'_{\rm CO}$(1–0) from Sun et al. (2014) instead of the limit from this work. In each panel, a representative error bar is shown that factors in the systematic errors, which could cause relative shifts between this work and the comparison sample (i.e. the conversion from $L_{\rm IR}$ into SFR and the error on the K Jy^{-1} conversion from APEX; see Sections 2.1 and 4). In the $\Delta_{\rm MS}$ column (right-hand panels), the median log-vertical distance from a linear fit to the Tacconi et al. (2018) non-AGN (green dashed line) is given. Our powerful CO-detected quasars, containing both outflows and jets, follow the overall trends seen in the comparison sample in all panels.

From these analyses, there is no evidence that the observed ionized outflows and jets in our powerful quasars have had an instantaneous impact on the observed CO luminosities.

5.1.2 *Molecular gas comparisons*

The more physically motivated quantities to study are the gas fraction (ratio of the molecular gas mass to stellar mass) and the depletion time (ratio of the molecular gas mass to the SFR), which relates to how efficiently stars are being formed for a given molecular gas mass. Based on large galaxy samples, these molecular gas properties scale with redshift, stellar mass, and distance from the star-forming galaxy main sequence (see e.g. Tacconi et al. 2018; Liu et al. 2019, and references therein). In this work, we are not concerned with the physical significance of these relations, but use them as a tool to compare the molecular gas properties of our sample to the wider galaxy population.

We compare our data to the homogenized sample of Tacconi et al. (2018) limited to within ±0.05 of the maximum and minimum redshift of our sample and only using their CO-based measurements.[11] Specifically, the data compiled come from the xCOLD GASS (Saintonge et al. 2017), EGNOG (Bauermeister et al. 2013), and GOALS (Armus et al. 2009) surveys and from the sample presented in Combes et al. (2011). We identified AGN hosts for each sample using BPT-based AGN classifications (the same as used to identify our sample; see Section 2), where available, and including all AGN classes (e.g. low-ionization nuclear emission-line regions, Seyferts, quasars, composite; Baldwin et al. 1981). The galaxies in this redshift-matched comparison sample span the complete range of stellar mass, sSFR, and $\Delta_{\rm MS}$ found for our sample (see Fig. 6).

To ensure consistency with the comparison sample, we calculate the molecular gas masses of our sample using the same procedure

[11] Combined CO(1–0) and (3–2).

as in Tacconi et al. (2018). Specifically, we follow the metallicity-dependent α_{CO} and mass–metallicity relation used by Tacconi et al. (2018) (see also Genzel et al. 2015) to calculate molecular gas masses following $M_{gas} = \alpha_{CO} \times L'_{CO}(1–0)$. The resultant α_{CO} values for our sample range from 4.0 to 4.2. We convert from $L'_{CO}(2–1)$ into $L'_{CO}(1–0)$ using $r_{21} = 0.8$. The full details of the equations used and a table of derived values are presented in Appendix B. For our seven CO(2–1) detected targets, the derived molecular gas masses fall in the range of $9.9 < \log(M_{gas}/M_\odot) < 10.5$, with corresponding ranges of gas fractions and depletion times of $M_{gas}/M_\star = 0.1–1.2$ and $M_{gas}/SFR = 0.16–0.95$ Gyr, respectively.

In Fig. 6, we compare our derived gas masses and depletion times to the Tacconi et al. (2018) population as a function of stellar mass, sSFR, and Δ_{MS}. We note that the dependence on the choice of main-sequence relation adds additional uncertainty to Δ_{MS} compared to sSFR; however, Δ_{MS} has been shown to be more closely related to the molecular gas properties (see e.g. Tacconi et al. 2018; Liu et al. 2019) and we obtain consistent conclusions if we just consider sSFR. Within errors, our sources overlap with the comparison sample (non-AGN and AGN) in all of the common diagnostic planes shown in Fig. 6. To quantify this comparison, we perform a simple log-linear fit to the Tacconi et al. (2018) sample with AGN removed (see Fig. 6). Our sample have a median log-vertical offset of +0.1 in the gas fraction versus Δ_{MS} plane and +0.04 in the depletion time versus Δ_{MS} plane (ignoring the non-detections).[12] This provides some evidence for moderately high (∼0.1 dex) gas fractions in our sample, with respect to their position relative to the main sequence. However, we cannot rule out that the two non-detected sources in our sample could bring our average down. Specifically, calculating the gas mass for J1356+1026 using the total $L'_{CO}(1–0)$ from Sun et al. (2014) would place it among the most gas-poor systems in the Tacconi et al. (2018) population, with a log-vertical distance from the Tacconi et al. (2018) line of −0.61 and −0.66 in gas fraction and depletion time, respectively (see Section 5.3).

The AGN included in Tacconi et al. (2018), which have no selection for high bolometric luminosity or outflows, go in the opposite direction to our CO-detected targets, with median log-vertical offsets of −0.12 in the gas fraction versus Δ_{MS} plane and −0.07 in the depletion time versus Δ_{MS} plane. We explore the possible role of AGN power further in Section 5.1.3.

It is important to consider possible systematic uncertainties in comparing AGN to non-AGN samples due to the assumptions required to calculate gas masses.[13] For example, there is no consensus on if AGN have systematically different ratios of $L'_{CO}(2–1)$ and (1–0), which is used to convert between the two (r_{21}; see e.g. Ocaña Flaquer et al. 2010; Papadopoulos et al. 2012; Xia et al. 2012; Husemann et al. 2017; Shangguan et al. 2020); however, we note that the observed range is modest ($0.4 < r_{21} < 1.2$) and we have adopted the mean value of 0.8 throughout this work (see e.g. Braine et al. 1993; Leroy et al. 2009). A larger uncertainty comes from α_{CO}, which, for most galaxies, appears to have a value of ∼4, with slight dependences on metallicity and SFR (see e.g. Bolatto et al. 2013; Sandstrom et al. 2013, and references therein). However, α_{CO} may be significantly lower in LIRGs, submillimetre galaxies, mergers, starbursts, and AGN (as low as ∼0.6; see e.g. Bolatto et al. 2013; Sargent et al. 2014; Calistro Rivera et al. 2018). In our comparison to literature results, we have controlled for many of these differences, i.e. we are comparing like-for-like in sSFR and Δ_{MS} and made consistent assumptions (see Appendix B). However, we cannot rule out some level of systematic differences in α_{CO} for AGN, which could shift our sources to systematically lower gas masses than the non-AGN comparison sample. Finally, we note that a limitation of our comparison to the Tacconi et al. (2018) catalogue is that it does not provide information on detection fractions or report upper limits. However, if anything, this limitation will strengthen our suggestion that the majority of the quasars in our sample, are comparatively gas-rich.

To summarize, although we cannot control for unknown systematic variations in α_{CO}, our quasar sample has molecular gas fractions and depletion times that are consistent with, or slightly higher than, the redshift matched comparison sample when considered in terms of their stellar masses, sSFRs, or distances to the main sequence. This implies no significant rapid depletion of the molecular gas supply despite the presence of kpc-ionized gas outflows and jets.

5.1.3 The impact of AGN on the molecular gas content

To investigate the relationship between AGN and the molecular gas content in more detail, we build upon the work of Saintonge et al. (2017), which found that the BPT selected AGN in the xCOLD GASS sample with the highest [O III]/Hβ ratios (taken as a proxy of the power of the AGN radiation field) tend towards higher gas fractions. In Fig. 7, we plot gas fractions as a function of the [O III]/Hβ ratio for both the xCOLD GASS sample and the quasars presented in this work. For a fair comparison with the Saintonge et al. (2017) data we, again, use $r_{21} = 0.8$, and follow their method to obtain α_{CO}. That is, we use the metallicity- and Δ_{MS}-dependent function of Accurso et al. (2017), which results in α_{CO} values between 3.3 and 6.0, and gas masses of $9.8 < \log(M_{gas}/M_\odot) < 10.5$ (for the seven detected targets; see Appendix B for full details).[14]

Fig. 7 reveals that our sample, extending to the most extreme local AGN, with no pre-selection on molecular gas or star-forming properties, agrees with and strengthens the previous results from xCOLD GASS: The more extreme AGN (i.e. those with log ([O III]/Hβ) $\gtrsim$0.6) tend to have the highest gas fractions. On average, for the combined samples, we find $(M_{gas}/M_\star)_{average} = 0.02$ for the sources with $\log([O\,III]/H\beta) < 0.6$ and $(M_{gas}/M_\star)_{average} = 0.16$ for the sources with $\log([O\,III]/H\beta) > 0.6$ (excluding non-detections). We note that a similar trend is observed for our sample when the bolometric AGN luminosity from our SED fits (see Jarvis et al. 2019) is used instead of [O III]/Hβ.

As highlighted by the colour-coding in Fig. 7, the most extreme AGN with the highest gas fractions are hosted in galaxies with high levels of concurrent star formation. Specifically, we find increasingly high Δ_{MS} values for increasing [O III]/Hβ values. Indeed, when considering instead of the gas fraction, the log-vertical offset of each AGN from linear fits to redshift and stellar mass matched Tacconi et al. (2018) samples in the gas fraction versus Δ_{MS} plane (see Section 5.1.2), the trend with [O III]/Hβ disappears. Specifically, the median vertical offset of the combined sample with

[12] Where the log-vertical offset for a point (a,b) from a line $y = f(x)$ with both in log space, is defined as $b - f(a)$.

[13] We also note that, although the Tacconi et al. (2018) work does not directly account for an AGN contribution to their stellar mass and SFR calculations, their sample does not include type 1 quasars and are typically low-power AGN (and therefore the AGN do not dominate the optical–UV part of the SEDs) so the impact is not expected to be strong.

[14] We note that J0945+1738, J1000+1242, and J1356+1026 are strong starbursts and might be better described with a lower α_{CO} (see Appendix B); however, this would not change our conclusions.

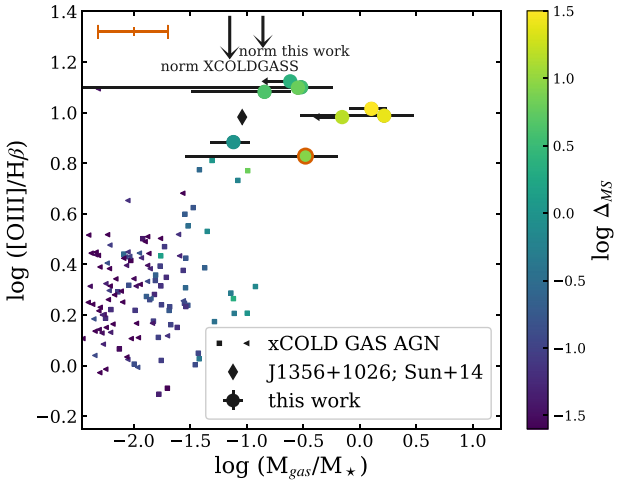

Figure 7. [O III] 5007 to H β emission-line ratio versus gas fraction ($M_{\rm gas}/M_\star$) of our quasars (circles) and xCOLD GASS AGN (squares, with triangles for upper limits; from the catalogues provided with Saintonge et al. 2017). The errors on the [O III]/H β ratios for our sample are smaller than the point size. A representative systematic error bar is shown in the top left-hand corner as in Fig. 6. J1010+0612 is highlighted with a red outline as per Fig. 5 and a black diamond marks the value for J1356+1026 using $L'_{\rm CO}$(1–0) from Sun et al. (2014) instead of the limit from this work. Data points are colour-coded by their distance to the Sargent et al. (2014) main sequence ($\Delta_{\rm MS}$). The two arrows show the average gas fraction from the Tacconi et al. (2018) sample matched in stellar mass and redshift to each population, to demonstrate that the observed trend is not dominated by differences in these parameters between the two samples. Sources with high [O III]/H β ratios tend to have high gas fractions and have sSFRs above the main sequence.

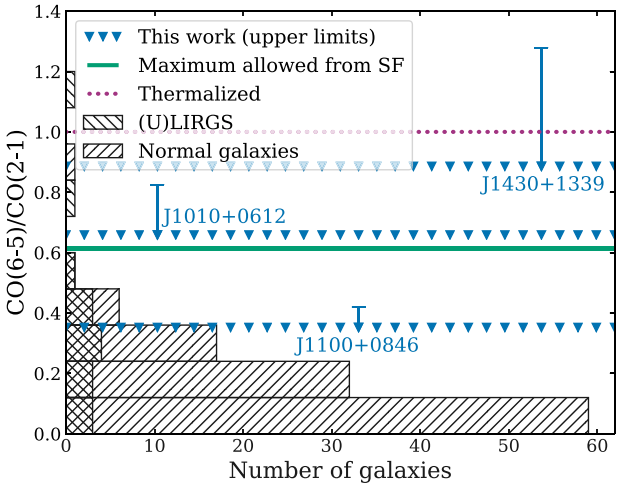

Figure 8. Upper limits of $L'_{\rm CO}$(6–5)/$L'_{\rm CO}$(2–1) ratios, for the three sources with these observations, represented as lines of blue triangles. Corresponding error bars represent the maximum values given the uncertainty on the measured CO(2–1) flux. The green line marks a maximum ratio achievable from star formation alone assuming a maximum SFR surface density of 1000 $M_\odot$ yr^{-1} kpc^{-2} following Narayanan & Krumholz (2014). The dotted magenta line marks where the molecular gas becomes thermalized. The histograms show the distribution of $L'_{\rm CO}$(6–5)/CO(2–1) ratios for literature galaxy samples from Papadopoulos et al. (2012) ([U]LIRGs only) and Kamenetzky et al. (2016). For at least two of our sources (J1010+0612 and J1100+0846), we do not have any evidence for highly excited CO SLEDs (see Section 5.2).

log([O III]/H β) <0.6 is −0.05, while the median value for the sources with log([O III]/H β) > 0.6 is ∼0 (see also Section 5.1.2 and Fig. 6). We note, however, that our sample covers a very narrow range of [O III]/H β and xCOLD GAS is not designed as an AGN survey and so, due to volume and redshift limits, does not contain any powerful AGN. Larger samples, uniformly covering AGN with a range of powers, would be needed to strengthen this observation. We discuss the impact of these results on the relationships between AGN activity, molecular gas masses, and SFRs in Section 5.3.

5.2 CO excitation

The relative luminosity of different CO lines contains information about the conditions of the molecular gas and the mechanisms that are exciting it. Through our APEX observations, we put constraints on the ratio of the CO(6–5) to the CO(2–1) luminosity ($L'_{\rm CO}$; r_{62}) for three sources in our sample. Specifically, we find $r_{62} < 0.66$, 0.35 and 0.89 for J1010+0612, J1100+0846, and J1430+1339 respectively (see Fig. 8). For J1010+0612, if an 18 per cent lower CO(2–1) flux is assumed to account for possible blending with its close companion, the limit on r_{62} increases marginally to 0.8 (which is within the error bar shown in Fig. 8).

The most ubiquitous source of CO excitation is photodissociation regions (PDRs) from the UV photons emitted from young stars. However, this mechanism is inefficient at exciting higher CO transitions. Shocks and/or X-ray emission (through X-ray-dominated region models, XDR), both of which can be powered by AGN or jets, are needed to further excite the CO gas (see e.g. Pereira-Santaella et al. 2013; Carniani et al. 2019).

The CO spectral line energy distribution (SLED) modelled by Narayanan & Krumholz (2014), which depends solely on the SFR surface density ($\Sigma_{\rm SFR}$), predicts values of $r_{62} \lesssim 0.24$ for typical SFR surface densities of $\lesssim$10 $M_\odot$ yr^{-1} kpc^{-2}, and even for an exceptionally high limit of $\Sigma_{\rm SFR} = 1000$ $M_\odot$ yr^{-1} kpc^{-2}, $r_{62} \gtrsim 0.6$ cannot be achieved. Our observed limit for J1100+0846 in particular suggests that the excitation of its total molecular gas could be explained by star formation alone, even at the highest end of the possible r_{62} ratio for this source. For J1010+0612, the observed limit of $r_{62} < 0.66$ could be explained by star formation alone; however, some contribution of shocks and XDR, possibly powered by the AGN, cannot be ruled out.

In Fig. 8, we also show the distribution of observed r_{62} ratios from Kamenetzky et al. (2016) and Papadopoulos et al. (2012). This shows that the majority of sources are consistent with their CO(6–5) emission being caused by PDR. However, for the galaxies with $r_{62} \gtrsim 0.24$, it is worth noting that their relatively excited state would require either fairly high SFR surface densities (>10 $M_\odot$ yr^{-1} kpc^{-2}) or imply the presence of another excitation mechanism (i.e. shocks or XDR). The three most extreme sources in these samples ($r_{62} \gtrsim 0.6$; IRAS 08572+3915 at 1.1, NGC 34 at 0.92, and 3C 293 at 0.78) all have a strong indication that AGN activity is responsible for the abnormally high r_{62} (see e.g. Emonts et al. 2005; Floyd et al. 2006; Papadopoulos et al. 2010; Cicone et al. 2014; Mingozzi et al. 2018). Our observed r_{62} limits on J1010+0612 and J1100+0846 can rule out such an extreme AGN excitation as seen in these sources. Unfortunately, our weaker limit on J1430+1339, which, of the three targets observed in CO(6–5), shows the clearest indications of jet activity (Jarvis et al. 2019), does not allow us to place any constraints on the excitation source for the CO(6–5) emission.

In summary, despite the fact that our targets containing kpc-scale ionized outflows (Fig. 1; Harrison et al. 2014; Jarvis et al. 2019), we

see no evidence that the CO emission is extremely excited based on the L'_{CO}(6–5)/CO(2–1) ratios. This result is not entirely unexpected. For example, Rosenberg et al. (2015) found that the IR colours of galaxies is a strong predictor of their CO excitation. Based on this, our galaxies (with IRAS 60/100 μm flux $\lesssim$1) should not have highly excited CO. Also, the effect of the AGN is expected to be most clearly seen at $J > 10$ (e.g. Mashian et al. 2015; Lu et al. 2017) or at extreme gas densities (e.g. Lamperti et al. 2020). Observations of higher CO transitions could provide a more complete constraint on the influence of the AGN (see e.g. van der Werf et al. 2010; Mashian et al. 2015; Carniani et al. 2019) and spatially resolved observations at multiple CO transitions would enable a study of any localized impact on the gas by the AGN or jets that could be undetectable in the total galaxy-wide emission (see e.g. Dasyra et al. 2016; Zhang et al. 2019).

5.3 The role of AGN in galaxy evolution

Many works have explored the total molecular gas content of AGN host galaxies compared to non-AGN galaxies (e.g. Simpson et al. 2012; Husemann et al. 2017; Kakkad et al. 2017; Perna et al. 2018; Rosario et al. 2018; Kirkpatrick et al. 2019; Shangguan et al. 2020); however, due to the huge amount of variation in the data used, the analysis conducted, and the different selection criteria for comparison samples, creating a unified picture of these results is challenging. The most consistent conclusion seems to be that the molecular gas content for low-redshift ($z \ll 1$) AGN populations is broadly consistent with matched non-AGN galaxies (see e.g. Xia et al. 2012; Krips, Neri & Cox 2012; Villar-Martín et al. 2013).[15] Our comparison to non-AGN samples generally supports these broad conclusions: We find, at most, moderate differences in observed or derived molecular gas properties for our quasar sample compared to galaxy samples matched in redshift, stellar mass, sSFR, and Δ_{MS} (see Figs 5 and 6). Additionally, our results suggest that powerful type 2 AGN with signatures of ionized gas outflows and jets reside preferentially in gas-rich starburst galaxies.

In Sections 5.1 and 5.2, we showed that in our sample of local quasars with kpc-ionized gas outflows and jets, there is no indication of AGN feedback having an immediate impact on the total gas reservoir once their distance to the star-forming main sequence is accounted for. These observations, however, are unable to rule out a more localized impact, which can sometimes be observed using spatially resolved molecular gas measurements (e.g. Salomé et al. 2017; Rosario et al. 2018; Fotopoulou et al. 2019; Ramakrishnan et al. 2019; Shin et al. 2019; Lutz et al. 2020). Furthermore, we can not rule out that these processes will have an impact on the global molecular gas supply on longer time-scales. Specific predictions of the typical spatial scales and time frames of the impact on the molecular gas reservoirs are required to test different AGN feedback models (see e.g. Lapi et al. 2014), which has already started to be investigated on host galaxy SFRs (see e.g. Harrison 2017; Scholtz et al. 2018; Schulze et al. 2019).

Figs 6 and 7 indicate that our quasars lie preferentially in molecular gas-rich systems even though our only pre-selections were on the width and luminosity of [O III] and radio luminosity. Indeed, these systems are more gas-rich, and are more likely to reside in starburst galaxies than less extreme AGN host galaxies (Fig. 7). This is also in qualitative agreement with recent work revealing a relationship between AGN power and offset from the main sequence (at least at $z \sim 1$; Bernhard et al. 2019; Grimmett et al. 2020). Although indirectly, our work is consistent with a link between AGN activity and star formation that is driven by the underlying gas content of the host galaxy. Furthermore, similar results have been found in works considering atomic gas and high-redshift sources (see e.g. Ellison et al. 2019; Rodighiero et al. 2019, respectively).

It is worth noting that one of our sources, which is undetected in our APEX data, may be exceptional in that it does have a low gas content. Using the Sun et al. (2014) CO(1–0) luminosity of $L'_{CO} = 1.03 \times 10^9$ K km s^{-1} pc^2 for J1356+1026 would put it amongst the most gas-poor sources in our comparison sample from Tacconi et al. (2018) (M_{gas}/SFR = 0.05 Gyr) and cause it to fall approximately four times lower than the Sargent et al. (2014) starburst relation (see Fig. 5). This implies either that the luminosity reported in Sun et al. (2014) does not detect all of the diffuse, low-surface-brightness CO emission, or could imply that this source is more rapidly quenched than the rest of our sample. The most obvious exceptional property of this source, which could impact its molecular gas content compared to the rest of the sample, is the double nuclei separated by $\sim$2.5 kpc (Greene, Zakamska & Smith 2012), indicating an ongoing merger.

Overall the observed high molecular gas masses and incidence of starbursts in our sample are consistent with the scenario where the AGN and star formation are linked, and is in broad agreement with simple evolutionary based AGN unification models (see e.g. Sanders et al. 1988; Hopkins et al. 2006; Hickox et al. 2009). Specifically, the well-studied scenario where gas-rich systems have high levels of star formation and obscured/type 2 AGN activity (possibly triggered by mergers), which is followed by feedback processes (such as outflows and jets) that will ultimately quench the AGN activity and star formation in the galaxy. Larger, less biased samples would be needed to confirm these models however. Although we can not be sure of the fate of our galaxies, we may have caught these systems in a special evolutionary phase where the feedback processes are just beginning. We can concretely conclude that the outflows and jets we observe do not *rapidly* remove the global molecular gas in an appreciable way (i.e. on a time-scale shorter than, or equal to, the observed quasars, jets, or outflows).

Our findings are consistent with many previous studies of the molecular gas and star formation in low-redshift AGN ($z \lesssim 0.2$). For example, Husemann et al. (2017) find gradually increasing amounts of molecular gas going from AGN in bulge-dominated to disc-dominated to major merger host galaxies and a trend to higher molecular gas masses in systems with more luminous AGN. Similarly, Bertram et al. (2007) find that the Seyferts in their sample have molecular gas content consistent with normal star-forming galaxies, while the powerful quasars are more consistent with starbursts. Luminous AGN are known to generally reside in galaxies with more recent star formation than their lower luminosity counterparts (see e.g. Balmaverde et al. 2016; Bernhard et al. 2019; Grimmett et al. 2020; Kim, Choi & Kim 2020). Finally, there is evidence that obscured AGN lie in more gas-rich systems than their unobscured counterparts (Wylezalek & Zakamska 2016; Rosario et al. 2018) and that the most extreme outflows may be preferentially found in rapidly star-forming, gas-rich systems (see e.g. Rodríguez Zaurín et al. 2013; Harrison et al. 2014; Wylezalek & Zakamska 2016).

To summarize, we find that our sample, selected to be luminous type 2 AGN hosting ionized outflows, lies preferentially in gas-rich galaxies, with high levels of simultaneous star formation, which is consistent with the evolutionary framework described above.

[15] The picture at high redshift is somewhat less clear (e.g. Kakkad et al. 2017; Perna et al. 2018; Rosario et al. 2018; Kirkpatrick et al. 2019; Circosta et al., in preparation)

However, the small size of this sample and the two non-detections limit our ability to expand these findings to the quasar population in general. By selecting systems with fast, prominent kpc-ionized gas outflows, we might have expected these outflows to be able to remove the molecular gas, resulting in a deficit. However, the data suggest that if these outflows or jets will ultimately have an impact on the global molecular gas content, it is subtle, or we have captured them too early in the feedback process for this effect to be measurable.

6 CONCLUSIONS

Using APEX observations of the CO(2–1) emission line, we have explored the global molecular gas content of nine $z \sim 0.1$ galaxies selected to host powerful type 2 quasars ($\log[L_{\rm AGN}/{\rm erg\,s^{-1}}] \gtrsim 45$) with galaxy-wide ionized outflows and radio jets (see Fig. 1; Harrison et al. 2014; Jarvis et al. 2019). We detected seven of the nine targets in CO(2–1), with corresponding $L'_{\rm CO}(2–1)$ values of (1.4–7)$\times 10^9$ K km s^{-1} pc^2. For a subset of three targets, we used APEX to obtain upper limits on the CO(6–5)/CO(2–1) emission-line ratios. Our main conclusions are as follows:

(i) For at least seven of the nine quasars in our sample, the total molecular gas reservoirs show no indication of being rapidly depleted due to AGN feedback, despite being selected to have powerful ionized gas outflows and jets. First, we find CO luminosities consistent (within 0.3 dex) with what would be predicted for the general galaxy population given their $L_{\rm IR}$ and distance to the star-forming main sequence (see Fig. 5 and Section 5.1.1). Secondly, the derived gas fractions and depletion times of our seven CO(2–1) detected sources (i.e. $M_{\rm gas}/M_\star \approx 0.1$–1.2 and $M_{\rm gas}$/SFR$\approx$0.16–0.95 Gyr, respectively) are comparable to those of redshift-matched non-AGN star-forming galaxies when taking into account their stellar mass, sSFR, and distance from the main sequence (see Fig. 6 and Section 5.1.2).

(ii) Galaxies hosting powerful AGN (i.e. $\log([{\rm O\,III}]/{\rm H}\,\beta) \gtrsim 0.6$) tend to have systematically higher gas fractions than those with less powerful AGN and star-forming galaxies in general, when our sample is considered together with those from the xCOLD GASS survey (Saintonge et al. 2017). Galaxies across these samples with the highest gas fractions appear to contain the most powerful AGN and highest levels of concurrent star formation (in relation to the star-forming main sequence; see Fig. 7 and Section 5.1.3).

(iii) The AGN are not having an extreme impact on the global CO excitation in at least two of the three sources for which we have upper limits on the $L'_{\rm CO}(2–1)$/CO(6–5) emission-line ratios (i.e. $r_{62} \lesssim 0.66$; see Fig. 8 and Section 5.2).

In summary, we find that the majority of our sample of quasars have gas-rich, starburst host galaxies, even though we did not select the sample based on these properties. Furthermore, we find that their gas masses are consistent with what would be expected for their observed levels of star formation. There are no signs of an instantaneous depletion of the total molecular gas reservoir by the AGN in our sample, despite their high bolometric luminosities, strong ionized gas outflows, and the presence of kpc-scale jets in many. Our results are consistent with a requirement for high molecular gas fractions to feed both quasar activity and intense periods of star formation. Indeed, by selecting luminous AGN with powerful ionized gas outflows, we may have predominantly selected galaxies in a phase in their evolution where intense star formation and AGN activity are powered by large molecular gas reservoirs and the 'feedback' in the form of jets and outflows is relatively young and these processes have not yet had any global impact upon the host galaxies.

Future, higher resolution CO observations and observations of more CO transitions will help determine if these processes have a more subtle and/or localized impact upon the molecular gas properties. Furthermore, galaxy formation models should work towards specific predictions of the molecular gas properties (e.g. gas fractions, depletion times, excitation) to compare to observations, such as ours, to aid understanding of the expected physical scales and time frames of any impact caused by different AGN feedback model prescriptions.

ACKNOWLEDGEMENTS

We thank the referee for their prompt and constructive comments. APEX is a collaboration between the Max-Planck-Institut für Radioastronomie, the European Southern Observatory, and the Onsala Observatory. PJ acknowledges funding from the European Research Council (ERC) under the European Union's Horizon 2020 research and innovation programme under grant agreement No 724857 (Consolidator Grant ArcheoDyn). DMA acknowledges the support of the UK Science and Technology Facilities Council (STFC) through grants ST/P000541/1 and ST/T000244/1.

DATA AVAILABILITY

The data underlying this paper were accessed from the ESO Science Archive Facility: http://archive.eso.org/eso/eso_archive_main.html under programme IDs E-0100.B-0166 and E-0104.B-0292. The derived data generated in this research will be shared on reasonable request to the corresponding author.

REFERENCES

Abazajian K. N. et al., 2009, ApJS, 182, 543
Accurso G. et al., 2017, MNRAS, 470, 4750
Alexander D. M., Hickox R. C., 2012, New Astron. Rev., 56, 93
Armus L. et al., 2009, PASP, 121, 559
Baldwin J. A., Phillips M. M., Terlevich R., 1981, PASP, 93, 5
Balmaverde B. et al., 2016, A&A, 585, A148
Bauermeister A. et al., 2013, ApJ, 768, 132
Belitsky V. et al., 2018, A&A, 612, A23
Bernhard E., Grimmett L. P., Mullaney J. R., Daddi E., Tadhunter C., Jin S., 2019, MNRAS, 483, L52
Bertram T., Eckart A., Fischer S., Zuther J., Straubmeier C., Wisotzki L., Krips M., 2007, A&A, 470, 571
Bieri R., Dubois Y., Rosdahl J., Wagner A., Silk J., Mamon G. A., 2017, MNRAS, 464, 1854
Bischetti M. et al., 2019, A&A, 628, A118
Bolatto A. D., Wolfire M., Leroy A. K., 2013, ARA&A, 51, 207
Braine J., Combes F., Casoli F., Dupraz C., Gerin M., Klein U., Wielebinski R., Brouillet N., 1993, A&AS, 97, 887
Brinchmann J., Charlot S., White S. D. M., Tremonti C., Kauffmann G., Heckman T., Brinkmann J., 2004, MNRAS, 351, 1151
Buat V. et al., 2015, A&A, 577, A141
Calistro Rivera G. et al., 2018, ApJ, 863, 56
Calistro Rivera G., Lusso E., Hennawi J. F., Hogg D. W., 2016, ApJ, 833, 98
Carilli C. L., Walter F., 2013, ARA&A, 51, 105
Carniani S. et al., 2019, MNRAS, 489, 3939
Chabrier G., 2003, PASP, 115, 763
Churazov E., Sazonov S., Sunyaev R., Forman W., Jones C., Böhringer H., 2005, MNRAS, 363, L91
Cicone C. et al., 2014, A&A, 562, A21
Cicone C., Brusa M., Ramos Almeida C., Cresci G., Husemann B., Mainieri V., 2018, Nat. Astron., 2, 176
Ciesla L. et al., 2015, A&A, 576, A10

Combes F., García-Burillo S., Braine J., Schinnerer E., Walter F., Colina L., 2011, A&A, 528, A124
Costa T., Rosdahl J., Sijacki D., Haehnelt M. G., 2018a, MNRAS, 473, 4197
Costa T., Rosdahl J., Sijacki D., Haehnelt M. G., 2018b, MNRAS, 479, 2079
Cresci G., Maiolino R., 2018, Nat. Astron., 2, 179
Daddi E. et al., 2007, ApJ, 670, 173
Daddi E. et al., 2015, A&A, 577, A46
Dasyra K. M., Combes F., Oosterloo T., Oonk J. B. R., Morganti R., Salomé P., Vlahakis N., 2016, A&A, 595, L7
Davies R. et al., 2020, preprint (arXiv:2003.06153)
Elbaz D. et al., 2007, A&A, 468, 33
Elbaz D. et al., 2011, A&A, 533, A119
Ellison S. L., Brown T., Catinella B., Cortese L., 2019, MNRAS, 482, 5694
Emonts B. H. C., Morganti R., Tadhunter C. N., Oosterloo T. A., Holt J., van der Hulst J. M., 2005, MNRAS, 362, 931
Fabian A. C., 2012, ARA&A, 50, 455
Faucher-Giguère C.-A., Quataert E., 2012, MNRAS, 425, 605
Floyd D. J. E., Perlman E., Leahy J. P., Beswick R. J., Jackson N. J., Sparks W. B., Axon D. J., O'Dea C. P., 2006, ApJ, 639, 23
Fluetsch A. et al., 2019, MNRAS, 483, 4586
Foreman-Mackey D., Hogg D. W., Lang D., Goodman J., 2013, PASP, 125, 306
Fotopoulou C. M., Dasyra K. M., Combes F., Salomé P., Papachristou M., 2019, A&A, 629, A30
Genzel R. et al., 2010, MNRAS, 407, 2091
Genzel R. et al., 2012, ApJ, 746, 69
Genzel R. et al., 2015, ApJ, 800, 20
Greene J. E., Zakamska N. L., Smith P. S., 2012, ApJ, 746, 86
Greve T. R. et al., 2014, ApJ, 794, 142
Grimmett L. P., Mullaney J. R., Bernhard E. P., Harrison C. M., Alexander D. M., Stanley F., Masoura V. A., Walters K., 2020, MNRAS, 495, 1392
Gruppioni C. et al., 2008, ApJ, 684, 136
Harrison C. M., 2017, Nat. Astron., 1, 0165
Harrison C. M., Alexander D. M., Mullaney J. R., Swinbank A. M., 2014, MNRAS, 441, 3306
Harrison C. M., Thomson A. P., Alexander D. M., Bauer F. E., Edge A. C., Hogan M. T., Mullaney J. R., Swinbank A. M., 2015, ApJ, 800, 45
Hickox R. C. et al., 2009, ApJ, 696, 891
Hopkins P. F., Hernquist L., Cox T. J., Di Matteo T., Robertson B., Springel V., 2006, ApJS, 163, 1
Husemann B., Davis T. A., Jahnke K., Dannerbauer H., Urrutia T., Hodge J., 2017, MNRAS, 470, 1570
Ishibashi W., Fabian A. C., 2015, MNRAS, 451, 93
Jarvis M. E. et al., 2019, MNRAS, 485, 2710
Kakkad D. et al., 2017, MNRAS, 468, 4205
Kamenetzky J., Rangwala N., Glenn J., Maloney P. R., Conley A., 2016, ApJ, 829, 93
Kamenetzky J., Rangwala N., Glenn J., 2017, MNRAS, 471, 2917
Karouzos M., Woo J.-H., Bae H.-J., 2016, ApJ, 819, 148
Kauffmann G. et al., 2003, MNRAS, 341, 33
Kennicutt Robert C. J., 1998, ApJ, 498, 541
Kennicutt R. C., Evans N. J., 2012, ARA&A, 50, 531
Kewley L. J., Ellison S. L., 2008, ApJ, 681, 1183
Kim M., Choi Y.-Y., Kim S. S., 2020, MNRAS, 491, 4045
King A., Pounds K., 2015, ARA&A, 53, 115
Kirkpatrick A., Sharon C., Keller E., Pope A., 2019, ApJ, 879, 41
Krips M., Neri R., Cox P., 2012, ApJ, 753, 135
Lamperti I. et al., 2020, ApJ, 889, 103
Lansbury G. B., Jarvis M. E., Harrison C. M., Alexander D. M., Del Moro A., Edge A. C., Mullaney J. R., Thomson A. P., 2018, ApJ, 856, L1
Lapi A., Raimundo S., Aversa R., Cai Z. Y., Negrello M., Celotti A., De Zotti G., Danese L., 2014, ApJ, 782, 69
Leroy A. K. et al., 2009, AJ, 137, 4670
Liu D. et al., 2019, ApJ, 887, 235
Lu N. et al., 2017, ApJS, 230, 1
Lutz D. et al., 2020, A&A, 633, A134
Madau P., Dickinson M., 2014, ARA&A, 52, 415
Mancini C. et al., 2011, ApJ, 743, 86
Mashian N. et al., 2015, ApJ, 802, 81
Mingozzi M. et al., 2018, MNRAS, 474, 3640
Morganti R., 2017, Frontiers Astron. Space Sci., 4, 42
Morganti R., Oosterloo T., Oonk J. B. R., Frieswijk W., Tadhunter C., 2015, A&A, 580, A1
Mukherjee D., Bicknell G. V., Sutherland R., Wagner A., 2016, MNRAS, 461, 967
Mullaney J. R., Alexander D. M., Fine S., Goulding A. D., Harrison C. M., Hickox R. C., 2013, MNRAS, 433, 622
Narayanan D., Krumholz M. R., 2014, MNRAS, 442, 1411
Noeske K. G. et al., 2007, ApJ, 660, L43
Noll S., Burgarella D., Giovannoli E., Buat V., Marcillac D., Muñoz-Mateos J. C., 2009, A&A, 507, 1793
Ocaña Flaquer B., Leon S., Combes F., Lim J., 2010, A&A, 518, A9
Oosterloo T., Morganti R., Tadhunter C., Raymond Oonk J. B., Bignall H. E., Tzioumis T., Reynolds C., 2019, A&A, 632, A66
Papadopoulos P. P., van der Werf P., Isaak K., Xilouris E. M., 2010, ApJ, 715, 775
Papadopoulos P. P., van der Werf P. P., Xilouris E. M., Isaak K. G., Gao Y., Mühle S., 2012, MNRAS, 426, 2601
Pereira-Santaella M. et al., 2013, ApJ, 768, 55
Perna M. et al., 2018, A&A, 619, A90
Pettini M., Pagel B. E. J., 2004, MNRAS, 348, L59
Ramakrishnan V. et al., 2019, MNRAS, 487, 444
Rodighiero G. et al., 2019, ApJ, 877, L38
Rodríguez Zaurín J., Tadhunter C. N., Rose M., Holt J., 2013, MNRAS, 432, 138
Rosario D. J. et al., 2018, MNRAS, 473, 5658
Rosenberg M. J. F. et al., 2015, ApJ, 801, 72
Saintonge A. et al., 2017, ApJS, 233, 22
Salim S. et al., 2007, ApJS, 173, 267
Salomé Q., Salomé P., Miville-Deschênes M.-A., Combes F., Hamer S., 2017, A&A, 608, A98
Sanders D. B., Soifer B. T., Elias J. H., Madore B. F., Matthews K., Neugebauer G., Scoville N. Z., 1988, ApJ, 325, 74
Sandstrom K. M. et al., 2013, ApJ, 777, 5
Santini P. et al., 2015, ApJ, 801, 97
Sargent M. T. et al., 2014, ApJ, 793, 19
Scholtz J. et al., 2018, MNRAS, 475, 1288
Schreiber C. et al., 2015, A&A, 575, A74
Schulze A. et al., 2019, MNRAS, 488, 1180
Shangguan J., Ho L. C., Bauer F. E., Wang R., Treister E., 2020, ApJS, 247, 15
Shin J., Woo J.-H., Chung A., Baek J., Cho K., Kang D., Bae H.-J., 2019, ApJ, 881, 147
Simpson J. M. et al., 2012, MNRAS, 426, 3201
Solomon P. M., Downes D., Radford S. J. E., Barrett J. W., 1997, ApJ, 478, 144
Speagle J. S., Steinhardt C. L., Capak P. L., Silverman J. D., 2014, ApJS, 214, 15
Sun A.-L., Greene J. E., Zakamska N. L., Nesvadba N. P. H., 2014, ApJ, 790, 160
Tacconi L. J. et al., 2018, ApJ, 853, 179
Thompson T. A., Fabian A. C., Quataert E., Murray N., 2015, MNRAS, 449, 147
Tremonti C. A. et al., 2004, ApJ, 613, 898
Vallini L., Tielens A. G. G. M., Pallottini A., Gallerani S., Gruppioni C., Carniani S., Pozzi F., Talia M., 2019, MNRAS, 490, 4502
van der Werf P. P. et al., 2010, A&A, 518, L42
Vassilev V. et al., 2008, A&A, 490, 1157
Veilleux S., Maiolino R., Bolatto A. D., Aalto S., 2020, A&AR, 28, 2
Villar-Martín M. et al., 2013, MNRAS, 434, 978
Wagner A. Y., Bicknell G. V., Umemura M., 2012, ApJ, 757, 136
Whitaker K. E. et al., 2014, ApJ, 795, 104
Wyder T. K. et al., 2007, ApJS, 173, 293
Wylezalek D., Zakamska N. L., 2016, MNRAS, 461, 3724
Xia X. Y. et al., 2012, ApJ, 750, 92
Zhang C.-P., Li G.-X., Zhou C., Yuan L., Zhu M., 2019, A&A, 631, A110
Zubovas K., King A., 2012, ApJ, 745, L34

SUPPORTING INFORMATION

Supplementary data are available at *MNRAS* online.

Figure A1. Corner plot showing all the one- and two-dimensional projections of the posterior probability distributions of our parameters for the APEX CO(2–1) data for J0945+1737.
Figure A2. Same as Fig. A1 but for J0958+1439.
Figure A3. Same as Fig. A1 but for J1000+1242.
Figure A4. Same as Fig. A1 but for J1010+1413.
Figure A5. Same as Fig. A1 but for J1010+0612.
Figure A6. Same as Fig. A1 but for J1100+0846.
Figure A7. Same as Fig. A1 but for J1316+1753.
Figure A8. Same as Fig. A1 but for J1356+1026.
Figure A9. Same as Fig. A1 but for J1430+1339.
Figure A10. Same as Fig. A1 but for the APEX CO(6–5) data for J1010+0612.
Figure A11. Same as Fig. A1 but for the APEX CO(6–5) data for J1100+0846.
Figure A12. Same as Fig. A1 but for the APEX CO(6–5) data for J1430+1339.

Please note: Oxford University Press is not responsible for the content or functionality of any supporting materials supplied by the authors. Any queries (other than missing material) should be directed to the corresponding author for the article.

APPENDIX A: BAYESIAN FITTING

This section provides further details about our Bayesian fits to our APEX CO observations. The values quoted in Table 3 are derived from these fits. The corner plots showing the posterior probability distributions of each of the parameters for each source are given in the online supplementary data ('Supplement to Appendix A'; Figs A1–A12).

For the seven CO(2–1) detected targets (see Section 4), we used initial guess parameters from reduced χ^2 Gaussian fits to the emission-line data using 100 km s^{-1} bins. For the initial guess parameters for the two CO(2–1) undetected targets (J0958+1439 and J1356+1026), we used the average σ (line width) from the detected targets (170 km s^{-1}) and $v_p = 0$. For J0958+1439, we chose an initial guess flux derived from the $L'_{\rm CO}$–$L_{\rm IR}$ starburst relation (see Section 5.1.1; $f \approx 6$ Jy km s^{-1}) and for J1356+1026, we used the Sun et al. (2014) ALMA CO(1–0) and CO(3–2) total fluxes for a rough estimate ($f \approx 6$ Jy km s^{-1}). For the initial guess parameters for fitting the CO(6–5) data, we used the values found through our Bayesian analysis for the CO(2–1) data, multiplying the fluxes by 1.4 to convert into the CO(6–5) transition (for typical LIRGs; Papadopoulos et al. 2012). By fitting sources multiple times with the initial guesses varied by approximately an order of magnitude, we confirmed that the results, within errors do not depend strongly on the initial guess used.

We adopted weak priors for our fitting procedure. We limited the flux and $\sigma_{\rm N}$ (noise) to be greater than zero, v_p, to be within $\pm$2000 km s^{-1} for CO(2–1) and $\pm$1500 km s^{-1} for the CO(6–5) data (i.e. the velocity coverage of the data). We constrained σ (line width) to be greater than zero and used slightly different maximum values of σ for different cases. Specifically, for the CO(2–1) detections, we limited the line width to be less than three times the width of the initial guess from the reduced χ^2 Gaussian fit (corresponding to upper values of 360–680 km s^{-1}), and for the non-detections, we used the largest limit from the detected lines (i.e. $\sigma \leq$680 km s^{-1}). For the CO(6–5) data, we limited σ (line width) to be less than three times the CO(2–1) line width from this Bayesian analysis (i.e. the values quoted in Table 3). We note that using more complicated or more constraining priors could lower the errors on our fits and our upper limits; however, this would risk introducing bias into the results.

Our fitting code is designed to be completely general and therefore, our likelihood is composed of a single Gaussian with both Poisson and Gaussian noise considered. However, Poisson and Gaussian likelihoods become indistinguishable even for very moderate values of the mean parameter (>10). Our priors are uniform distributions that drop to 0 outside of the bounds described above. We use 100 walkers for the MCMC analysis and run it for 500 steps with the first 300 steps later cropped as burn in (visual inspection of the trace plots were used to confirm the burn in period for all fits). We determine the starting position for each walker using the initial guesses described above with a random offset added drawn from a uniform distribution limited to within $\pm$ 3 orders of magnitude less than the initial guess.

For each source where the CO(2–1) line is detected (all except J0958+1439 and J1356+1026), the posterior distributions for all four parameters show clear peaks. In contrast, the non-detections do not show clear peaks in one or more of the parameters (the posteriors for σ in particular do not have clear peaks for any of the non-detected CO lines; see corner plots in online 'Supplement to Appendix A'). Further details on the individual fits can be found in the corner plots and captions in Figs A1–A12.

APPENDIX B: $\alpha_{\rm CO}$ AND MOLECULAR GAS MASS CALCULATIONS

Here we provide specific details about how we calculated $\alpha_{\rm CO}$ and the molecular gas masses. We also present these derived values for each source, using the two different methods that are discussed in this paper (see Table B1). In each case, $r_{21} = 0.8$ is used to convert from CO(2–1) into CO(1–0) (see Section 5.1.2).

For a comparison with the values from Tacconi et al. (2018) (Section 5.1.2 and Fig. 6), we follow the $\alpha_{\rm CO}$ calculation from that work (as in Genzel et al. 2015), taking the geometric mean of the metallicity-dependent $\alpha_{\rm CO}$ recipes of Bolatto et al. (2013) and Genzel et al. (2012):

$$\alpha_{\rm CO} = 4.36 \times \sqrt{\begin{array}{r} 0.67 \times \exp(0.36 \times 10^{-1\times(12+\log({\rm O/H})-8.67)} \\ \times 10^{(-1.27\times(12+\log({\rm O/H})-8.67)}) \end{array}}, \quad \text{(B1)}$$

where $\alpha_{\rm CO}$ has units M$_\odot$ (K km s^{-1} pc^2)$^{-1}$. Also, following Tacconi et al. (2018), we use the following mass metallicity relation from Genzel et al. (2015):

$$12 + \log({\rm O/H}) = a - 0.087 \times (\log M_\star - b)^2, \quad \text{(B2)}$$

where $a = 8.74$ and

$$b = 10.4 + 4.46 \times \log(1+z) - 1.78 \times (\log(1+z))^2. \quad \text{(B3)}$$

For the comparison with the xCOLD GASS samples in Section 5.1.3, we calculate $\alpha_{\rm CO}$ following Saintonge et al. (2017). Specifically, they use the metallicity- and $\Delta_{\rm MS}$-dependent $\alpha_{\rm CO}$ correlation from Accurso et al. (2017):

$$\begin{aligned} \log \alpha_{\rm CO} = {} & 14.752 - 1.623 \times [12 + \log(({\rm O/H})] \\ & + 0.062 \times \log \Delta_{\rm MS}. \end{aligned} \quad \text{(B4)}$$

To keep consistent with the methods adopted in the comparison sample, we calculate the metallicity (12+log(O/H)) following the Pettini & Pagel (2004) 'O3N2' consistent mass–metallicity relation

Table B1. The values α_{CO} and M_{gas} for each source in this sample using the two methods used in this work to be consistent with the literature comparisons.

	Tacconi et al. comparison (Fig. 6)		xCOLD GASS comparison (Fig. 7)	
Name (1)	α_{CO} (2)	log $M_{gas}/M_\odot$ (3)	α_{CO} (4)	log $M_{gas}/M_\odot$ (5)
J0945+1737	4.1	$10.07^{+0.1}_{-0.08}$	5.3	$10.18^{+0.1}_{-0.08}$
J0958+1439	4.0	<10.0	3.4	<10.0
J1000+1242	4.2	$9.99^{+0.08}_{-0.06}$	6.0	$10.14^{+0.08}_{-0.06}$
J1010+1413	4.1	$10.54^{+0.07}_{-0.06}$	3.7	$10.5^{+0.07}_{-0.06}$
J1010+0612	4.0	$10.03^{+0.1}_{-0.09}$	3.9	$10.01^{+0.1}_{-0.09}$
J1100+0846	4.0	$10.15^{+0.08}_{-0.06}$	3.7	$10.1^{+0.08}_{-0.06}$
J1316+1753	4.1	10.1 ± 0.2	3.7	10.1 ± 0.2
J1356+1026	4.0	<10.0	3.9	<10.0
J1430+1339	4.1	$9.9^{+0.2}_{-0.1}$	3.3	$9.8^{+0.2}_{-0.1}$

Notes. (1) Object name; (2) α_{CO} calculated to be consistent with Tacconi et al. (2018); (3) log M_{gas} calculated to be consistent with Tacconi et al. (2018); (4) α_{CO} calculated to be consistent with xCOLD GASS (Saintonge et al. 2017); (5) log M_{gas} calculated to be consistent with xCOLD GASS (Saintonge et al. 2017).

of Kewley & Ellison (2008):

$$12 + \log(\mathrm{O/H}) = a + b \times \log M_\star + c \times \log M_\star^2 + d \times \log M_\star^3, \quad \text{(B5)}$$

where $a = 32.1488$, $b = -8.512\,58$, $c = 0.976\,384$, $d = -0.035\,9763$, and $M_\star$ is in $M_\odot$. For additional consistency we do not use the Δ_{MS} (i.e. the ratio of the sSFR of the galaxy and its local main sequence) derived in the main paper, but re-calculate this value for use in the α_{CO} calculation, using the same method as in Saintonge et al. (2017). That is, using the star-forming main sequence from Accurso et al. (2017):

$$\log \mathrm{sSFR_{MS}[Gyr]} = -1.12 + 1.14 \times z - 0.19 \times z^2 - (0.3 + 0.13 \times z)(\log M_\star - 10.5). \quad \text{(B6)}$$

As described in Accurso et al. (2017), this α_{CO} relation is only valid within $7.9 < 12+\log(\mathrm{O/H}) < 8.8$ and $-0.8 < \log\Delta_{MS} < 1.3$. Using the Δ_{MS} values for these calculations, J0945+1737, J1000+1242, and J1356+1026 all fall outside (or at the edge of) of the allowed Δ_{MS} range (with log $\Delta_{MS} = 1.6$, 1.4, and 1.3, respectively). However, using the recommended starburst α_{CO} from Accurso et al. (2017) of one for these sources does not change the conclusions of this work.

We note that the gas masses derived from both of the methods described above are consistent within errors.

This paper has been typeset from a TEX/LATEX file prepared by the author.

List of astronomical key words (Updated on 2020 January)

This list is common to *Monthly Notices of the Royal Astronomical Society, Astronomy and Astrophysics*, and *The Astrophysical Journal*. In order to ease the search, the key words are subdivided into broad categories. No more than *six* subcategories altogether should be listed for a paper.

The subcategories in boldface containing the word 'individual' are intended for use with specific astronomical objects; these should never be used alone, but always in combination with the most common names for the astronomical objects in question. Note that each object counts as one subcategory within the allowed limit of six.

The parts of the key words in italics are for reference only and should be omitted when the keywords are entered on the manuscript.

General
editorials, notices
errata, addenda
extraterrestrial intelligence
history and philosophy of astronomy
miscellaneous
obituaries, biographies
publications, bibliography
sociology of astronomy
standards

Physical data and processes
acceleration of particles
accretion, accretion discs
asteroseismology
astrobiology
astrochemistry
astroparticle physics
atomic data
atomic processes
black hole physics
chaos
conduction
convection
dense matter
diffusion
dynamo
elementary particles
equation of state
gravitation
gravitational lensing: micro
gravitational lensing: strong
gravitational lensing: weak
gravitational waves
hydrodynamics
instabilities
line: formation
line: identification
line: profiles
magnetic fields
magnetic reconnection
(magnetohydrodynamics) MHD
masers
molecular data
molecular processes
neutrinos
nuclear reactions, nucleosynthesis, abundances
opacity
plasmas
polarization
radiation: dynamics
radiation mechanisms:general
radiation mechanisms: non-thermal
radiation mechanisms: thermal
radiative transfer
relativistic processes
scattering
shock waves
solid state: refractory
solid state: volatile
turbulence
waves

Astronomical instrumentation, methods and techniques
atmospheric effects
balloons
instrumentation: adaptive optics
instrumentation: detectors
instrumentation: high angular resolution
instrumentation: interferometers
instrumentation: miscellaneous
instrumentation: photometers
instrumentation: polarimeters
instrumentation: spectrographs
light pollution
methods: analytical
methods: data analysis
methods: laboratory: atomic
methods: laboratory: molecular
methods: laboratory: solid state
methods: miscellaneous
methods: numerical
methods: observational
methods: statistical
site testing
space vehicles
space vehicles: instruments
techniques: high angular resolution
techniques: image processing
techniques: imaging spectroscopy
techniques: interferometric
techniques: miscellaneous
techniques: photometric
techniques: polarimetric
techniques: radar astronomy
techniques: radial velocities
techniques: spectroscopic
telescopes

Astronomical data bases
astronomical data bases: miscellaneous
atlases
catalogues
surveys
virtual observatory tools

Software
software: data analysis
software: development
software: documentation
software: public release
software: simulations

Astrometry and celestial mechanics
astrometry
celestial mechanics
eclipses
ephemerides
occultations
parallaxes
proper motions
reference systems
time

The Sun
Sun: abundances
Sun: activity
Sun: atmosphere
Sun: chromosphere
Sun: corona
Sun: coronal mass ejections (CMEs)
Sun: evolution
Sun: faculae, plages
Sun: filaments, prominences
Sun: flares
Sun: fundamental parameters
Sun: general
Sun: granulation
Sun: helioseismology
Sun: heliosphere
Sun: infrared
Sun: interior
Sun: magnetic fields
Sun: oscillations
Sun: particle emission
Sun: photosphere
Sun: radio radiation
Sun: rotation
(Sun:) solar–terrestrial relations
(Sun:) solar wind
(Sun:) sunspots
Sun: transition region
Sun: UV radiation
Sun: X-rays, gamma-rays

Planetary systems
comets: general

comets: individual: . . .
Earth
interplanetary medium
Kuiper belt: general

Kuiper belt objects: individual: . . .
meteorites, meteors, meteoroids
minor planets, asteroids: general

minor planets, asteroids: individual: . . .
Moon
Oort Cloud
planets and satellites: atmospheres
planets and satellites: aurorae
planets and satellites: composition
planets and satellites: detection
planets and satellites: dynamical evolution and stability
planets and satellites: formation
planets and satellites: fundamental parameters
planets and satellites: gaseous planets
planets and satellites: general

planets and satellites: individual: . . .
planets and satellites: interiors
planets and satellites: magnetic fields
planets and satellites: oceans
planets and satellites: physical evolution
planets and satellites: rings
planets and satellites: surfaces
planets and satellites: tectonics
planets and satellites: terrestrial planets
planet–disc interactions
planet–star interactions
protoplanetary discs
zodiacal dust

Stars
stars: abundances
stars: activity
stars: AGB and post-AGB
stars: atmospheres
(stars:) binaries *(including multiple)*: close
(stars:) binaries: eclipsing
(stars:) binaries: general
(stars:) binaries: spectroscopic
(stars:) binaries: symbiotic
(stars:) binaries: visual
stars: black holes
(stars:) blue stragglers
(stars:) brown dwarfs
stars: carbon
stars: chemically peculiar
stars: chromospheres
(stars:) circumstellar matter
stars: coronae
stars: distances
stars: dwarf novae
stars: early-type
stars: emission-line, Be
stars: evolution
stars: flare
stars: formation
stars: fundamental parameters
(stars:) gamma-ray burst: general
(stars:) **gamma-ray burst: individual: . . .**
stars: general
(stars:) Hertzsprung–Russell and colour–magnitude diagrams
stars: horizontal branch
stars: imaging
stars: individual: . . .
stars: interiors

stars: jets
stars: kinematics and dynamics
stars: late-type
stars: low-mass
stars: luminosity function, mass function
stars: magnetars
stars: magnetic field
stars: massive
stars: mass-loss
stars: neutron
(stars:) novae, cataclysmic variables
stars: oscillations *(including pulsations)*
stars: peculiar *(except chemically peculiar)*
(stars:) planetary systems
stars: Population II
stars: Population III
stars: pre-main-sequence
stars: protostars
(stars:) pulsars: general
(stars:) **pulsars: individual: . . .**
stars: rotation
stars: solar-type
(stars:) starspots
stars: statistics
(stars:) subdwarfs
(stars:) supergiants
(stars:) supernovae: general
(stars:) **supernovae: individual: . . .**
stars: variables: Cepheids
stars: variables: Scuti
stars: variables: general
stars: variables: RR Lyrae
stars: variables: S Doradus
stars: variables: T Tauri, Herbig Ae/Be
(stars:) white dwarfs
stars: winds, outflows
stars: Wolf–Rayet

Interstellar medium (ISM), nebulae
ISM: abundances
ISM: atoms
ISM: bubbles
ISM: clouds
(ISM:) cosmic rays
(ISM:) dust, extinction
ISM: evolution
ISM: general
(ISM:) HII regions
(ISM:) Herbig–Haro objects

ISM: individual objects: . . .
(except planetary nebulae)
ISM: jets and outflows
ISM: kinematics and dynamics
ISM: lines and bands
ISM: magnetic fields
ISM: molecules
(ISM:) photodissociation region (PDR)
(ISM:) planetary nebulae: general
(ISM:) **planetary nebulae: individual: . . .**
ISM: structure
ISM: supernova remnants

The Galaxy
Galaxy: abundances
Galaxy: bulge
Galaxy: centre
Galaxy: disc
Galaxy: evolution
Galaxy: formation
Galaxy: fundamental parameters
Galaxy: general
(Galaxy:) globular clusters: general
(Galaxy:) **globular clusters: individual: . . .**
Galaxy: halo
Galaxy: kinematics and dynamics
(Galaxy:) local interstellar matter
Galaxy: nucleus
(Galaxy:) open clusters and associations: general
(Galaxy:) **open clusters and associations: individual: . . .**
(Galaxy:) solar neighbourhood
Galaxy: stellar content
Galaxy: structure

Galaxies
galaxies: abundances
galaxies: active
galaxies: bar
(galaxies:) BL Lacertae objects: general
(galaxies:) **BL Lacertae objects: individual: . . .**
galaxies: bulges
galaxies: clusters: general

galaxies: clusters: individual: . . .
galaxies: clusters: intracluster medium
galaxies: disc
galaxies: distances and redshifts
galaxies: dwarf
galaxies: elliptical and lenticular, cD
galaxies: evolution
galaxies: formation
galaxies: fundamental parameters
galaxies: general
galaxies: groups: general

galaxies: groups: individual: . . .
galaxies: haloes
galaxies: high-redshift

galaxies: individual: . . .
galaxies: interactions
(galaxies:) intergalactic medium
galaxies: irregular
galaxies: ISM
galaxies: jets
galaxies: kinematics and dynamics
(galaxies:) Local Group
galaxies: luminosity function, mass function
(galaxies:) Magellanic Clouds
galaxies: magnetic fields
galaxies: nuclei
galaxies: peculiar
galaxies: photometry
(galaxies:) quasars: absorption lines
(galaxies:) quasars: emission lines
(galaxies:) quasars: general

(galaxies:) **quasars: individual: . . .**
(galaxies:) quasars: supermassive black holes
galaxies: Seyfert
galaxies: spiral
galaxies: starburst
galaxies: star clusters: general

galaxies: star clusters: individual: . . .
galaxies: star formation
galaxies: statistics
galaxies: stellar content
galaxies: structure

Cosmology
(cosmology:) cosmic background radiation
(cosmology:) cosmological parameters
(cosmology:) dark ages, reionization, first stars
(cosmology:) dark energy
(cosmology:) dark matter
(cosmology:) diffuse radiation
(cosmology:) distance scale
(cosmology:) early Universe
(cosmology:) inflation
(cosmology:) large-scale structure of Universe
cosmology: miscellaneous
cosmology: observations
(cosmology:) primordial nucleosynthesis
cosmology: theory

Resolved and unresolved sources as a function of wavelength
gamma-rays: diffuse background
gamma-rays: galaxies
gamma-rays: galaxies: clusters
gamma-rays: general
gamma-rays: ISM
gamma-rays: stars
infrared: diffuse background
infrared: galaxies
infrared: general
infrared: ISM
infrared: planetary systems
infrared: stars
radio continuum: galaxies
radio continuum: general
radio continuum: ISM
radio continuum: planetary systems
radio continuum: stars
radio continuum: transients
radio lines: galaxies
radio lines: general
radio lines: ISM
radio lines: planetary systems
radio lines: stars
submillimetre: diffuse background
submillimetre: galaxies
submillimetre: general
submillimetre: ISM
submillimetre: planetary systems
submillimetre: stars
ultraviolet: galaxies
ultraviolet: general
ultraviolet: ISM
ultraviolet: planetary systems
ultraviolet: stars
X-rays: binaries
X-rays: bursts
X-rays: diffuse background
X-rays: galaxies
X-rays: galaxies: clusters
X-rays: general
X-rays: individual: . . .
X-rays: ISM
X-rays: stars

Transients
(transients:) black hole mergers
(transients:) black hole - neutron star mergers
(transients:) fast radio bursts
(transients:) gamma-ray bursts
(transients:) neutron star mergers
transients: novae
transients: supernovae
transients: tidal disruption events